Current physical picture of the stagnation process and state in MDD, LDD and LID

Radha Bahukutumbi[1], Jeremy Chittenden[7], Johan Frenje[2] (chair), Joseph Kilkenny[9], Patrick Knapp[4], Jim Knauer[1], Roberto Mancini[8], Thomas Murphy[5], Pravesh Patel[3], Kyle Peterson[4], Sean Regan[1] (co-chair), Andrew Schmitt[6,] Andrei Simakov[5], Brian Spears[3], Paul Springer[3] and Alexander Velikovich[6]

[1]Laboratory for Laser Energetics, University of Rochester
[2]Massachusets Institute of Technology
[3]Lawrence Livermore National Laboratory
[4]Sandia National Laboratories
[5]Los Alamos National Laboratory
[6]Naval Research Laboratory
[7]Imperial College, London
[8]University of Nevada, Reno
[9]General Atomics

NISP FY16 Report submitted to National Nuclear Security Administration

Contents

1. Introduction

1.1 Goals with the National Inertial Confinement Fusion (ICF) Program

As stated in the 2016 Inertial Confinement Fusion Program (ICF) Framework [1.1], the principal goals with the ICF Program in 2020 are:

- For Magnetic Direct Drive (MDD), demonstrate 100 kJ DT equivalent yield, or understand why if unable to do so.
- For Laser Direct Drive (LDD), first, demonstrate an inferred hot-spot pressure of 100 Gbar, or understand why if unable to do so. Secondly, understand Laser-Plasma-Interaction (LPI) mitigation and control at the ignition length scale.
- For Laser Indirect Drive (LID), demonstrate the efficacy of the NIF for achieving ignition, or understand why if unable to do so.

For each approach (shown in Figure 1.1), the goal is also to determine the credible physics scaling to multi-mega-joule fusion yields. A key challenge though is to demonstrate that ICF has indeed achieved these goals and that the program is on the path of achieving them. A "demonstration" has been achieved by generating a quantitative assessment of the state of the 'stagnated' plasma; providing an explanation of measured deviations from calculated performance; and understanding the underlying assumptions for physics-scaling arguments and associated uncertainties.

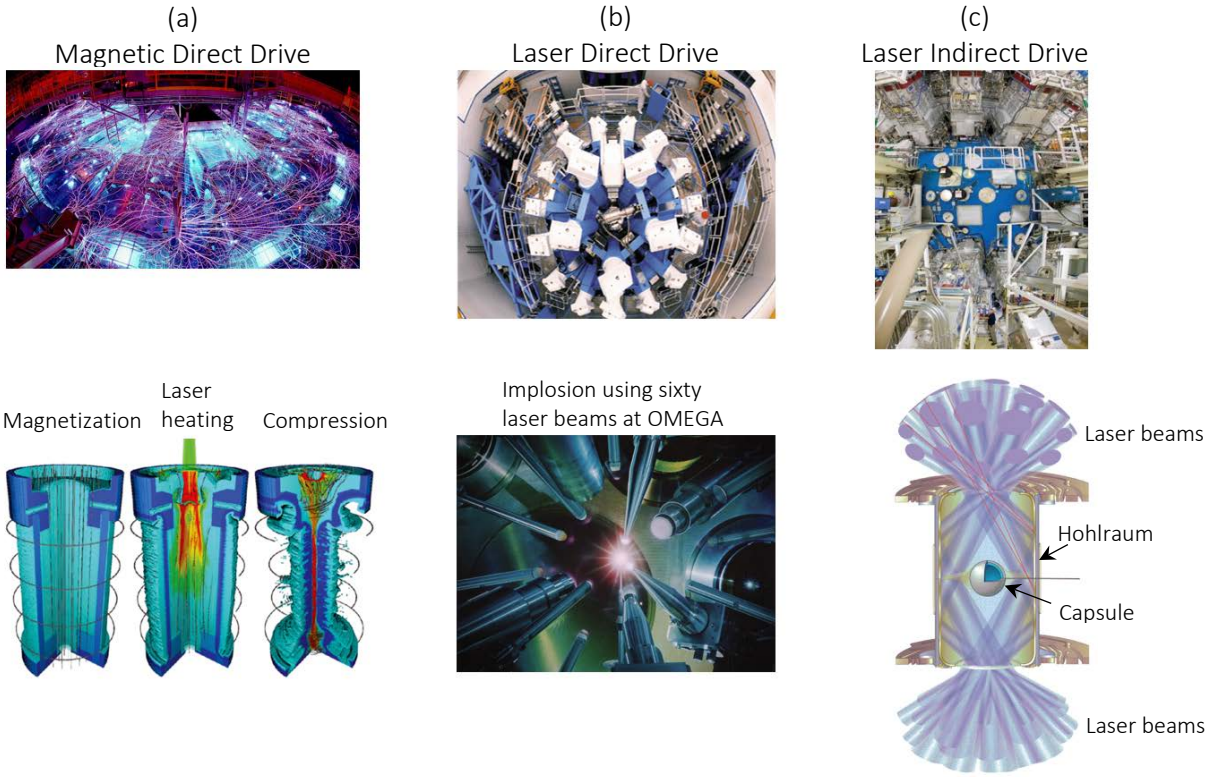

Figure 1.1. The three main approaches used in the National ICF program. (a) Magnetic Direct Drive (MDD) at the Z facility at Sandia National Laboratory [1.2]. (b) Laser Direct Drive (LDD) at the OMEGA laser facility at Laboratory for Laser Energetics, University of Rochester [1.3]. (c) Laser Indirect Drive (LID) at the National Ignition Facility at Lawrence Livermore National Laboratory [1.4].

1.2 Remarks on stagnation

In the context of ICF, stagnation has traditionally been thought of as the state of maximum fuel compression where the kinetic energy of the implosion has been converted into hot-spot thermal energy. Ideally, this process creates a hot stagnation phase when the hot-spot temperature reaches a maximum and the Residual Kinetic Energy (RKE) reaches a minimum. In reality, the 'stagnated' plasma generally remains highly dynamic and three-dimensional (3D) in nature, the RKE is significant and many processes are still evolving. To address this issue and mitigate and control the 3D behavior, an improved understanding of the underlying physics governing the 'stagnation' process is required. As it is prohibitive to simultaneously determine the energy distribution of all particles as a function of space and time in an ICF implosion, an understanding of a 'stagnated' plasma is formed through an ensemble of integrating diagnostic observables that are described by simplified models utilizing physics approximations. Understanding these models and their applicability to the stagnation phase of an ICF implosion that is 3D and highly dynamic is a major factor determining whether ignition can be achieved in the near term or what is required to do so.

1.3 The National Implosion Stagnation Physics (NISP) Working group

To improve our understanding of the underlying physics of 'stagnation', NNSA established the National Implosion Stagnation Physics (NISP) Working Group in summer 2015. The FY16 goal for the NISP Working Group is to define a "peer-reviewed", physical picture of the 'stagnated' fuel and ablator/liner for MDD, LDD and LID. In particular, the NISP Working group should:

1. For each approach, describe a "peer-reviewed", distilled physical picture of the stagnated fuel and ablator/liner that is consistent with most data.
2. For each approach, define a list of "peer-reviewed" hypotheses for explaining the observations or discrepancies between observations and models.
3. For each approach, define a list of new "peer-reviewed" diagnostics, experiments and analyses methods needed to distinguish/refute the different hypotheses.

1.4 Function of the NISP Working group

The function of the NISP Working Group is to "peer-review" the updates made to this document, which will be done through workshops that focus on deliverables 1, 2 or 3 discussed above. It will be a living document that illustrates the progress each approach has made. In FY17 and beyond, more focused workshops will be held to scrutinize and to provide a deeper assessment of a particular topic such as the differences neutron-measured ion-temperature (thermal in MDD, near-isotropic and affected by bulk-fluid motion in LID and non-isotropic and affected by bulk-fluid motion in LDD). The ultimate goal of this multi-year NISP effort is to understand and chart the physics-scaling to multi-MJ yields for the three approaches in FY20.

2. 'Stagnation' in Magnetic Direct Drive (MDD)

2.1 The MDD concept

The Magnetized Liner Inertial Fusion (MagLIF) concept [2.1], shown in Figure 2.1, is the primary MDD fusion concept being explored at Sandia National Laboratories. This concept uses pulsed power to implode a cylindrical liner filled with pre-magnetized, preheated low-density deuterium gas. It relies on efficient, clean deposition of laser energy into the gas, effective magnetic insulation of the gas during implosion and efficient conversion of kinetic to thermal energy at stagnation. To date, the maximum measured DD neutron yield is 3×10^{12} and is consistent with thermonuclear production [2.2].

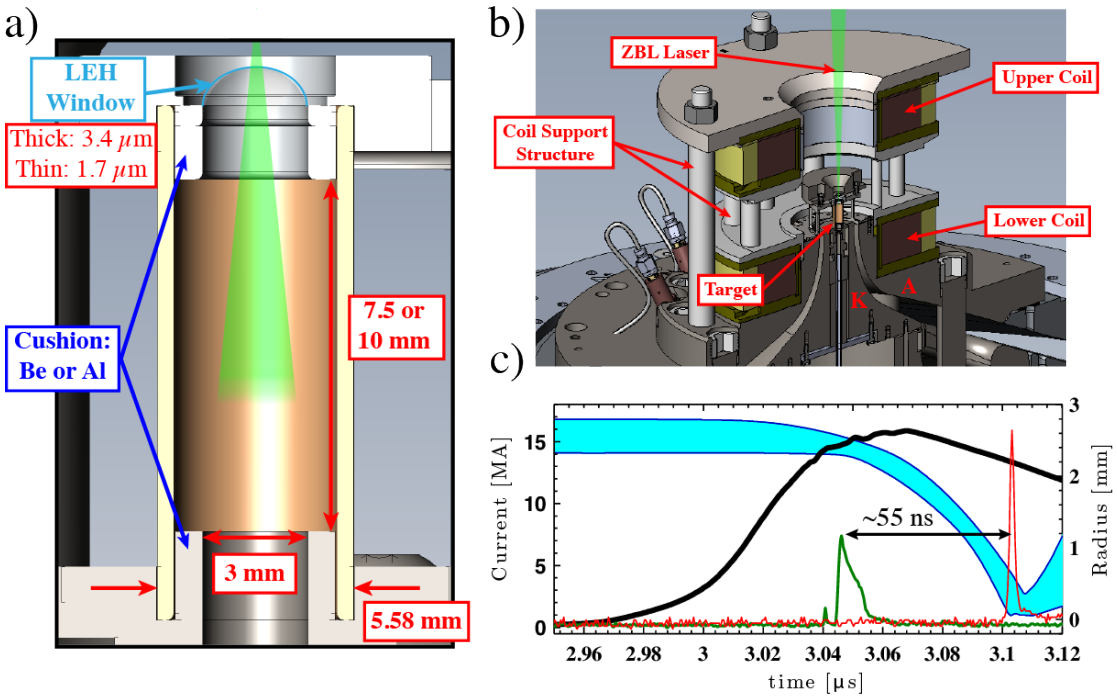

Figure 2.1. (a) Depiction of a typical MagLIF target identifying the Laser-Entrance Hole (LEH) window and cushions. (b) View of the MagLIF target and load hardware, including the B-field coils and final power-feed. (c) Typical current pulse (black solid curve) and one-dimensional (1D) liner trajectory (blue band). X-ray pulses are shown in green and red to indicate the time period of preheat and stagnation, respectively.

2.2 Physical picture of the stagnated fuel and liner

Our current understanding of stagnation is somewhat limited by available diagnostics, but a consistent picture is emerging. 2-3 keV electron temperatures (T_e) measured using x-ray spectroscopy are consistent with 2-2.5 keV ion temperatures (T_i) measured using neutron time-of-flight (nTOF) detectors. Measurements of the primary DD neutron spectrum and yield from different directions show excellent agreement, indicating isotropic neutron production. An example of nTOF spectra recorded axially and radially on the same shot are shown in Figures 2.2a and 2.2b. The inferred T_i values differ by ~10% between these views, which are well within the measurement uncertainty (<20%). Additionally, as shown in Figure 2.2c, the neutron yield scales with T_i as would be expected from a thermal plasma.

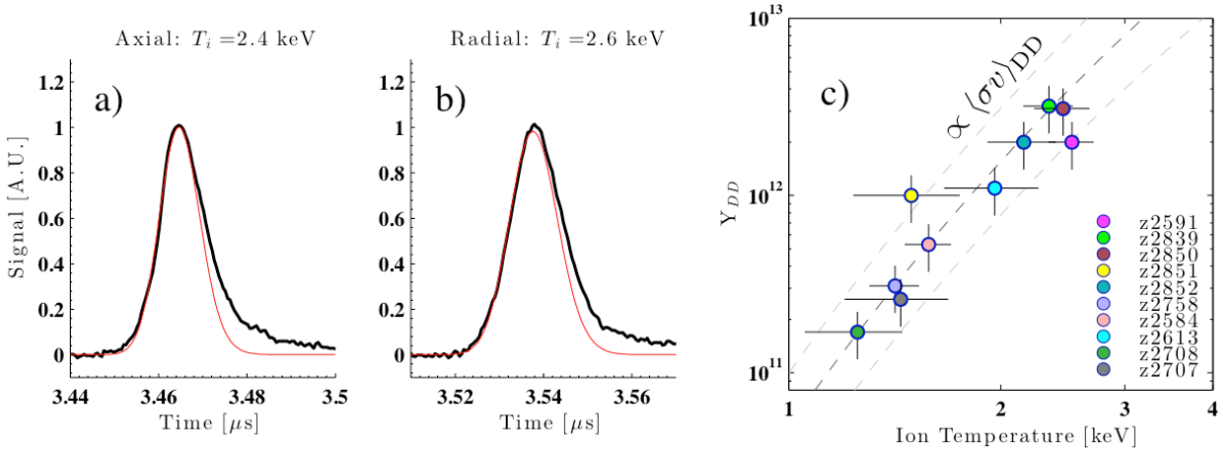

Figure 2.2. Demonstration of a thermonuclear plasma. (a) nTOF spectrum recorded axially, from beneath the target, with best fit and inferred T_i. (b) nTOF spectrum recorded on the same shot, but from the radial direction. Best fit T_i is in close agreement to the axial result, indicating isotropic neutron production. (c) DD neutron yield versus T_i for ten MagLIF shots, spanning a variety of target configurations. For comparison, the dashed curves illustrate the scaling of the DD fusion reactivity.

The fuel density at stagnation is inferred to be ~0.3 g/cc, however uncertainties are large (+/- 50%) due to ambiguities in how this quantity is inferred. These include a poorly understood mix fraction and emission volume. A burn width of 1.5-2 ns (FWHM) is inferred from x-ray power measurements, which assumes that the width of high-energy x-ray emission (hv > 9 keV) is sufficiently similar to the width of neutron emission. Combining this information with the DD neutron yield and/or x-ray yield, we find that the stagnation pressure is ~0.8-1 Gbar for the highest performing shots [2.3], compared to ~2 Gbar from calculations. The pressure inferred using different methods is consistent within uncertainties (e.g. x-rays and neutrons)

One interpretation of Figure 2.2c is that the ion density is constant across experiments with widely varying performance. However, as the neutron yield is proportional to the product of volume, burn width and density squared, this figure implies that this product is constant. The reasons for this are not immediately clear, however one possible interpretation is that 3D effects limit compression, regardless of the experiment. Measurements of volume and burn width tell us that these quantities vary by ~30% across different types of target implosions. In the future, improvements in both the measurement techniques and models used to interpret them will help elucidate this trend.

Additionally, we find that the magnetic field-radius product (BR) is 0.25-0.4 MG·cm at stagnation. This was determined using a novel technique, which exploits the effect of magnetic trapping of 1-MeV tritons on the observed secondary DT neutron yield and spectra shown in Figure 2.3 [2.4, 2.5]. This level of magnetization corresponds to an increase of approximately 17× over the initial BR and indicates that ~30-60% of the initial field is retained at stagnation, consistent with predictions, and is sufficient to trap the 1-MeV tritons produced by DD fusion reactions. This also implies that in a DT plasma, the ratio of plasma radius (R) to α-particle gyro radius (r_α) is R/r_α =1-1.5, indicating that α-particles are effectively confined at stagnation.

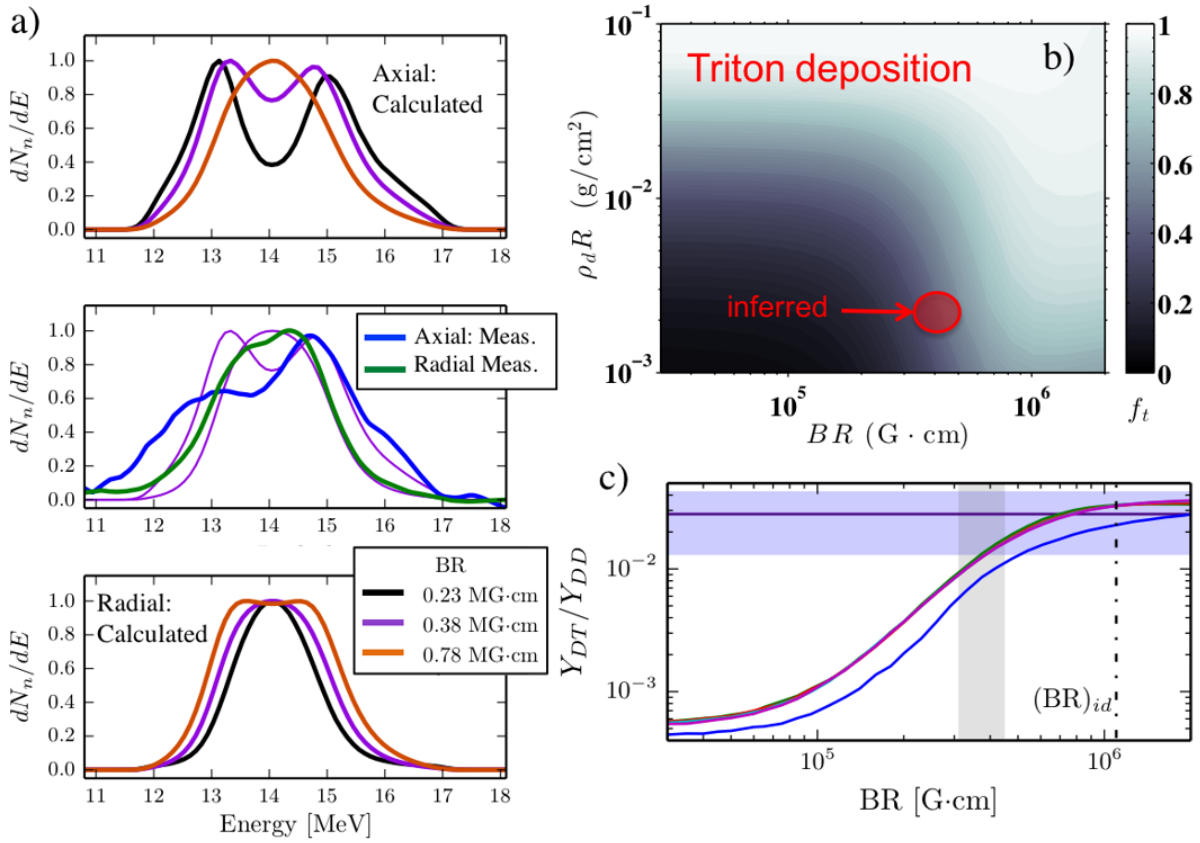

Figure 2.3. Demonstration that 1-MeV tritons, from DD reactions, are significantly magnetized. (a) Calculated and measured DT neutron spectra corresponding to shot z2591. The middle panel shows the measured (blue and green) and best-fit calculated (purple) spectra. The top and bottom panels show secondary DT neutron spectra viewed axially and radially, respectively, with varying *BR*. (b) A contour plot showing the fraction of the triton energy deposition (f_t) as a function of *BR* and ρR. The red circle indicates the inferred *BR* and ρR values from this particular shot, indicating a triton-energy deposition of >30%. (c) Variation in the secondary-DT-to-primary-DD yield ratio (Y_{DT}/Y_{DD}) as a function of *BR*. From this yield ratio, a *BR* value of 0.3-0.45 MG·cm was inferred for this shot.

Despite the fact that a self-consistent stagnation picture that describes the experimental observables has been developed, we have not yet been able to generate a completely self-consistent simulation model that agrees with all of the experimental observables. In general, neutron yields are approximately 2-10× lower than expected from quasi-1D simulations where the axial dimension is coarsely resolved to account for end losses, but not instabilities (this must imply a pressure deficit and 3D effects because the temperatures observed cannot explain the reduction in yield) – [2.9]. The yield-over-clean is highly sensitive to the amount of preheat energy assumed deposited into the gas. As detailed below, some combination of assumed preheat energy, mix and 3D effects at stagnation are the most likely effects limiting the performance, however, the balance between these effects is currently unknown. Additionally, target changes expected to improve performance have, in some cases, degraded performance. At a fundamental level, the energy balance in a MagLIF implosion is significantly uncertain as discussed in Figure 2.4. The dominant source dictating this uncertainty is the lack of understanding of the fuel-plasma conditions immediately after the laser heating. The three existing main hypotheses that explain the degraded

performance are all based on this: poor laser-energy coupling, laser-induced mix, and 3D effects at stagnation. Each of these hypotheses, along with their associated evidence will be detailed below. It is important to note that, while these hypotheses are stated individually, it is likely that each of these effects could be playing a significant role in the quality of stagnation depending on the target design and laser parameters. The goal of this exercise is to determine the balance between the different hypotheses and to determine the most important effects that need mitigation strategies. Additionally, there are other effects that may contribute to the degraded performance, but they are believed to be less significant. Some of these will also be addressed.

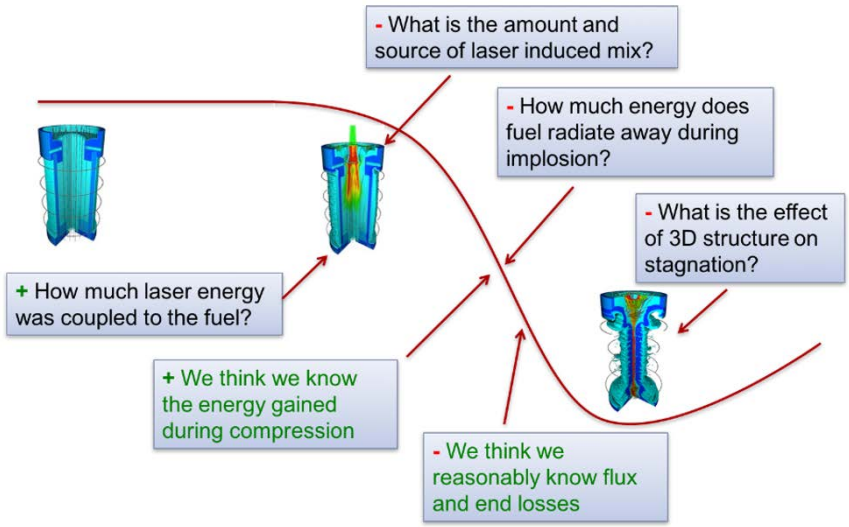

Figure 2.4. List of the systematic uncertainties and questions currently being explored in terms of energy balance.

2.3 Current state of modeling and simulation/data discrepancies

The 2D HYDRA and LASNEX codes have been the primary simulation tools used to design and analyze MagLIF experiments [2.6]. 3D analysis has also been performed using the GORGON code. The 2D simulations estimate the stagnation pressure to be 1.5 Gbar, with densities (0.4 g/cc) and temperatures (3.0 keV), which are somewhat higher than measured, but still within experimental uncertainties. In terms of shape and burn width, the simulated x-emission is also in agreement with experimental data. However, key assumptions are required to constrain these simulations.

In 1D and 2D simulations, the parameter that has the most significant impact on the results (in the absence of pre-imposed mix) is the amount of laser energy deposited into the gas during heating. All of the high-performing integrated MagLIF implosions to date have not employed any type of laser beam smoothing. The spatial profile of the laser beam is highly non-uniform with large intensity variations. Separate laser-only experiments have shown that a substantial (not yet quantified) portion of the laser light is backscattered due to LPI [2.7]. Our hydrodynamic codes have no means to self-consistently model the laser absorption and penetration that accounts for all possible loss mechanisms (e.g. LPI). Rather than exploring kinetic treatments and simulations of laser heating processes, the focus has been on mitigating the presence of LPI as much as possible through target design and laser configuration.

Because of these complications concerning laser interactions, 2D LASNEX and HYDRA simulations generally assume that only a small fraction of the energy is absorbed in the gas (typically 10-20 % of the

incident beam energy). These simulations are able to match many of the experimental observables within uncertainties while exhibiting a mix-free (no laser-induced mix) and effectively 1D implosion (1D in the sense that 1D stagnation pressures are obtained uniformly along the axis when mass losses are accounted for). A small fraction of the incident beam energy absorbed in the fuel is supported by several independent measurements, which will be detailed in the hypotheses sections. It is further hypothesized that the large knobs (laser energy and beam diameter) that must be tuned in our simulations to match the observables are a result of the unconditioned laser beam used in these experiments producing large amounts of LPI during the laser-target interaction. With high levels of LPI, it seems unlikely to obtain a predictive capability even with higher fidelity kinetic simulations. Therefore, we have prioritized the implementation of a distributed phase plate (DPP) in our experiments since a smoothed laser beam should be closer to what is assumed in our hydrodynamic simulations and could improve code predictability.

GORGON simulations are similarly consistent with the experimental observables if a much higher percentage of the laser energy is assumed to be absorbed into the fuel. In these simulations, a non-uniform stagnation, 3D in nature, is shown to reduce the average stagnation pressure and reduce the DD neutron yields by ~10×. This degradation is a result of azimuthal liner asymmetries that penetrate the hot spot that could cause quenching, inefficient thermalization and reduced confinement. Obviously, in the presence of 3D asymmetries, 2D simulations will over predict the convergence, plasma confinement, and efficiency of converting kinetic to thermal energy. Although significant progress has been made in measuring and generating remarkably stable implosions of MagLIF liners inflight, the absolute level of 3D asymmetries at stagnation and its impact on performance is uncertain. In-flight radiographs of the inner liner-wall structure are currently obtained in the absence of preheating (same laser is used) and images have only been obtained up to CR ~8 in a standard MagLIF configuration.

While the reduced laser coupling or non-uniform stagnation hypothesis rely heavily on inferences made through simulation comparisons, measured x-ray spectra do show signs of mix up to a few percent level [2.3] This is diagnosed at stagnation, although it could be introduced either during stagnation or earlier in time during laser preheat. This mix is known to come from Be and Al components that face the fuel, and also likely from the LEH window. This mix has been demonstrated to degrade performance, since when aluminum fuel facing components were replaced with beryllium ones the neutron yield was seen to increase. In light of this evidence of mix, a fair question to ask is whether or not the observables that can be matched using clean low-preheat, or non-uniform stagnation simulations represent unique solutions. This is an area that has not yet been fully explored due to the added complexity and free-parameters associated with modeling dynamic mix.

2.3.1 Hypothesis #1 for degraded performance: Only 10-20% laser energy coupling to the gas

Very little laser energy is coupled to the gas (10-20% of the incident beam energy). As the stagnation temperature and pressure are proportional to the initial temperature and pressure, this results in degraded performance. For instance, assuming no enhanced losses a 2× increase of preheat energy coupled to the gas results in roughly twice the initial temperature and therefore twice the stagnation temperature. For the DD reactivity, this implies an increase of ~10× in the neutron yield. Due to the complexity of quantifying laser energy deposited in the gas many of the inferences of low laser coupling rely on simulation comparisons to surrogate experiments that sometimes differ significantly from the MagLIF configuration. Efforts to characterize laser deposition in more closely matched experiments are currently underway.

Evidence:

- Dedicated laser heating experiments using the conditioned ZBL laser (no DPP) indicate poor laser transmission through the LEH window and subsequent poor coupling to the fuel as shown in Figure 2.5.
    - Calorimetric measurements of laser transmission through plastic foils showed only 10% transmission (~200 J) with similar thickness of LEH window (3.5 μm) as used in the initial integrated MagLIF experiments. However, as scatter-plate measurements indicate a significant amount of energy is scattered sideways out of the finite collection angle of the calorimeter, this energy represents a lower bound on transmission. When the pre-pulse was removed, no laser transmission through the foil was observed.
    - Time dependent optical-shadowgraph measurements of the laser blast wave in a Ne gas cell target (250 torr Ne target with 1 μm thick polyimide window and a 1-mm diameter focus) are comparable to simulations when 600 J of energy is assumed to be coupled to the fuel
    - VISAR velocity measurements of the laser blast wave interacting with the inner walls of a MagLIF target agree with simulations at several different axial heights when only 330 J is assumed to be coupled to the target with 120 psi DD gas and 3.5 μm LEH window. However, these calculations are 1D reconstructions matching only the radial motion at specific heights, and thus neglect the axial motion and azimuthal asymmetries in the blast wave. Furthermore, additional probes from the experiment did show large azimuthal asymmetries at lower axial heights (not shown here). Best focus of the laser was also on the LEH window, whereas best focus was 3.5 mm above the target in MagLIF experiments increasing the spot diameter from ~200 microns to ~500 microns and reducing its intensity. Successful MagLIF experiments have also used approximately half the gas fill density used here.
    - Backscatter measurements reveal that a significant, but uncertain, amount of energy is scattered by the LEH window and/or gas. Time resolved spectroscopy indicates that SBS is an important mechanism in the laser interaction with the window (SRS is not currently measured).

Imaging and spectroscopy of laser-only experiments reveal a shorter than expected laser penetration depth (as determined by the length of the heated plasma column) and lower than expected temperatures. Recent simulations of experiments using a 1.5-μm thick LEH window qualitatively match the laser propagation depth, radial size, and inferred T_e for a series of laser preheating experiments assuming that only 185 J of laser energy was coupled and a ~3× larger beam diameter on the window than prescribed. The chosen beam diameter is loosely based on the observations of the time dependent optical shadowgraphy measurements at the beginning of the main laser pulse, in addition to being tuned to match experimental observables of several different types of experiments. It is posited that LPI effects are spreading the effective beam profile during the initial interaction with the LEH window in some unknown manner. It should be noted that since these experiments were diagnosed with time-integrated emission diagnostics that view an argon dopant through a 100 micron beryllium, emission from plasmas with $T_e <$ 300 eV will not be observed. As such, if LPI effects cause the beam to filament or refract to large radii, the

lower temperature plasma produced may not be detectable, yet could contain a significant fraction of the energy deposited. Estimates made from comparison with this data may represent a lower bound on the energy deposited in the gas. Future experiments using a neon dopant will hopefully better characterize the distribution of energy in lower temperature plasmas.

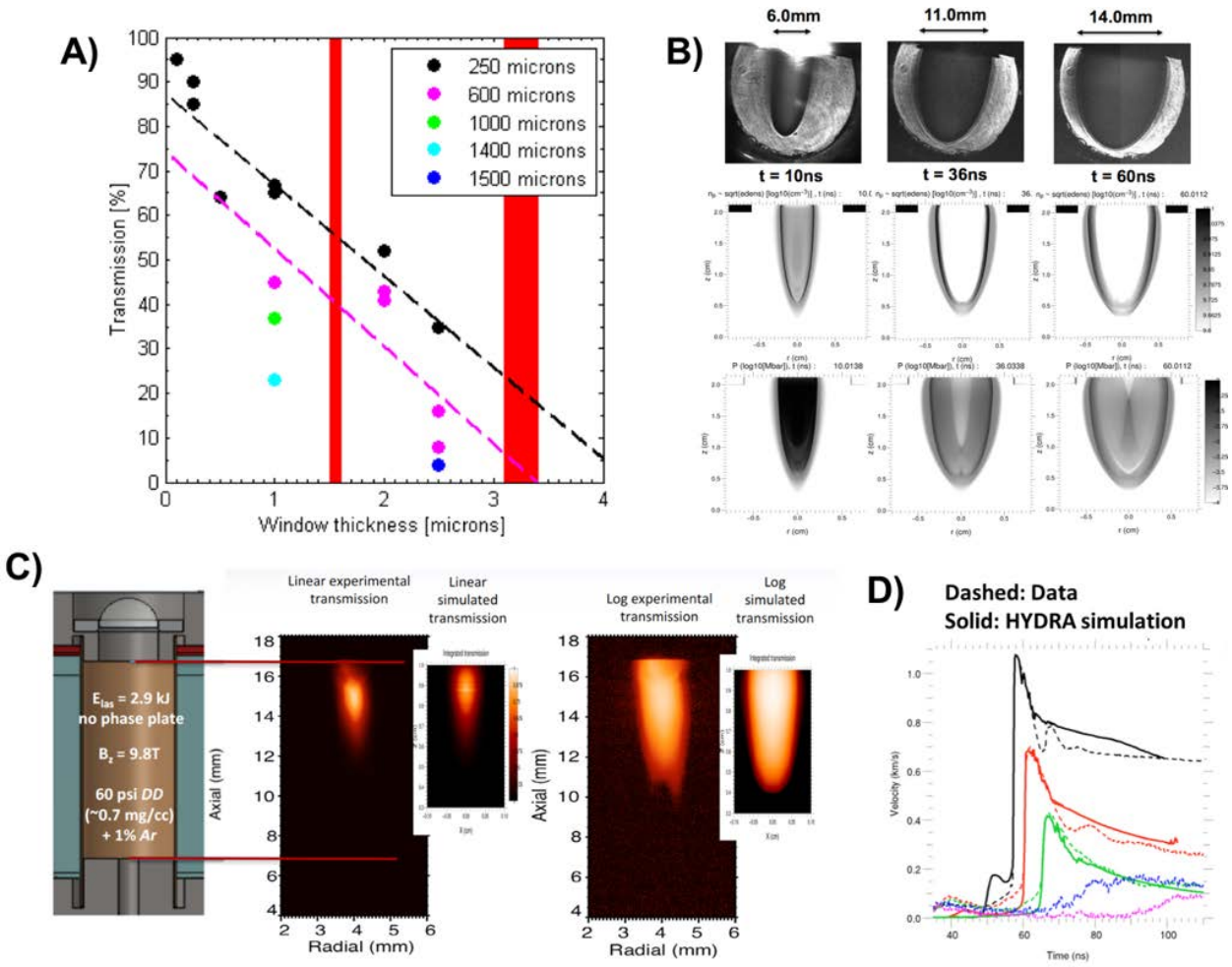

Figure 2.5. Four separate laser heating experiments with the Z-beamlet laser that show poor laser energy coupling to the gas. A) Measurements of laser transmission through foil vs. foil thickness. Red vertical bands represent equivalent LEH window thickness used in the integrated MagLIF experiments. Different colors represent defocusing to different beam diameters. B) Optical shadowgraph data from blast-wave measurements in 250 Torr of Ne gas with a 1 μm thick Mylar window made a different times after the rise of the ZBL laser pulse. Simulated images of the blast wave evolution at equivalent times assuming only 600 J coupled to the fuel in the second row. Third row represents iso-contours of the simulated pressure. C) Self emission measurements at Z of magnetized laser heating of ~3100 Torr D_2+1% Ar through thin-walled surrogate targets. Simulated comparisons assume only 200 J of energy coupled to the gas. D) VISAR measurements of the laser blast wave interacting with the target wall. Measurements were made at several different axial and azimuthal locations. The best match (shown) to the axial measurements assumes 330 J of energy coupled to the gas.

Initial laser heating experiments with a 0.75 and 1.1 mm DPP showed improvements in laser propagation and suggest higher energy coupling, particularly when the beam intensity was reduced. However, simulations cannot yet fully reproduce the data without adjusting experimental parameters, though the comparison is significantly improved compared to the high intensity no-DPP case. It is interesting to note that separate laser heating propagation experiments performed at OMEGA-EP and NIF have demonstrated agreement with the same simulation model while assuming no loss of laser energy [2.8]. However, OMEGA-EP experiments used a pure argon gas fill, while NIF experiments employed neo-pentane gas fill with thin (<1 μm-thick) LEH windows, so direct surrogacy to MagLIF experiments is limited. Additional OMEGA-EP data from more relevant Ar-doped deuterium gas-fill experiments have been obtained, although a detailed comparison to simulations has not yet been made. The pulse shape and laser intensities in both experiments are similar, but not identical. A significant difference between these and the ZBL experiments is the wavelength of laser light. ZBL is 2ω while OMEGA-EP and NIF are 3ω laser systems. This difference will be the subject of investigations in FY17.

2.3.2 Hypothesis #2 for degraded performance: Significant amount of mix

Some amount of the window, end cap, and/or liner material mixes into the gas primarily during the preheat phase. This results in enhanced radiative losses, which removes energy from the plasma during the relatively long time between preheat and stagnation (~50 ns). The end result is degraded pressure and reduced DD neutron yield at stagnation due to lower than predicted T_i.

Evidence:

- X-ray spectroscopy reveals Fe mixed into the hot spot at ~ppm levels, corresponding to a Be mix fraction of ~1%. The XRS3 x-ray spectrometer is able to measure K-shell emission from extremely low levels of Fe, allowing diagnosis of the hot-spot T_e and density as well as the mix fraction, if the concentration of Fe in the bulk Be is known. See Figure 2.6.
- Some filtered pinhole images of the preheated plasma are consistent with mix from the LEH window being present during the time of preheat.
- MagLIF implosions with Be cushions and thin (~1.5 μm thick) LEH windows produced ~10× higher DD neutron yields and exhibited T_i values ~2× higher than that of MagLIF implosions with Al cushions and same LEH windows. MagLIF implosions with Be cushions and thick LEH windows (3.4 μm) showed a more modest improvement in DD neutron yield (1.5-2×) and T_i (~20%). This indicates that removing mid-Z contaminants from the target is important, but the resulting effect is dependent on the LEH window thickness. This makes sense if the amount of mix is dependent on how much laser energy is transmitted through the window, thereby suggesting that a significant amount of mix is introduced during the laser-heating phase. See Figure 2.7.
- When similar MagLIF implosions but with different LEH window thicknesses (1.5 and 3.4 μm) are compared, the implosions with thicker window appears to perform better (by ~5-10×) when Al end caps/cushions are used. In contrast, implosions with thinner window show better performance (~3×) than implosions with thick windows when all target components in contact with the fuel are Be. This suggests that improving laser coupling by reducing the window thickness may exacerbate mix incurred at the preheat stage. See Figure 2.7.

- An experiment where the LEH window was moved closer to the fuel showed significantly lower performance than the baseline cases where the window is further away. This experiment produced low yield, very dim imaging and spectroscopy data, and no usable neutron spectral data. All these observations are indicative of the stagnation being too cold to produce useful signals (T_i < 1keV).
- An experiment with DPP to smooth the laser beam performed worse than similar implosions using an unconditioned beam. Spectroscopic evidence from stagnation shows a higher level of continuum emission relative to implosions that used an unconditioned beam, suggesting window mix was exacerbated (the window is CH and will contribute to continuum emission in the energy range of interest, but will not produce any line emission that can be used to identify it unambiguously).

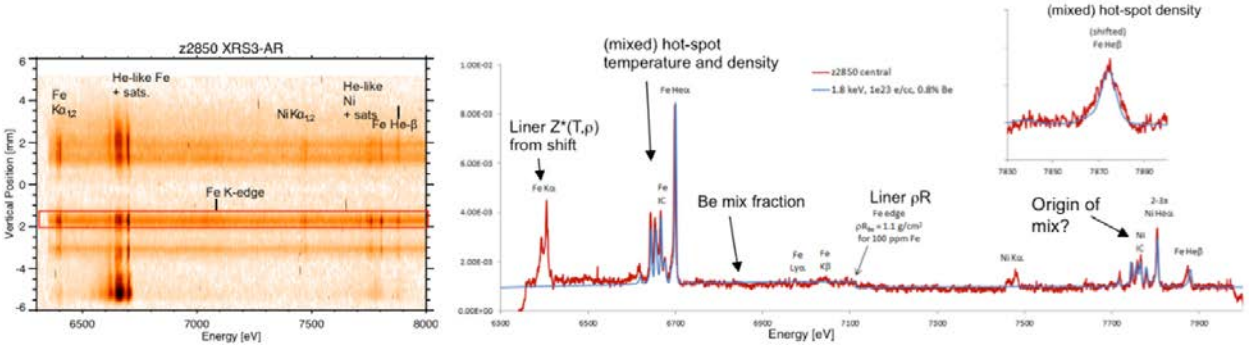

Figure 2.6. Demonstration of Fe mixed into the hot spot. Left panel shows the x-ray spectrum recorded using the XRS3 x-ray spectrometer on shot z2850. The bright lines are from Fe impurities in the Be liner and cushions that have mixed into the hot spot. Right panel shows a lineout from the measured spectrum as well as a fit to the data indicating a T_e of 1.8 keV and an electron density of 10^{23} cm^{-3} with a Be mix fraction of 0.8%.

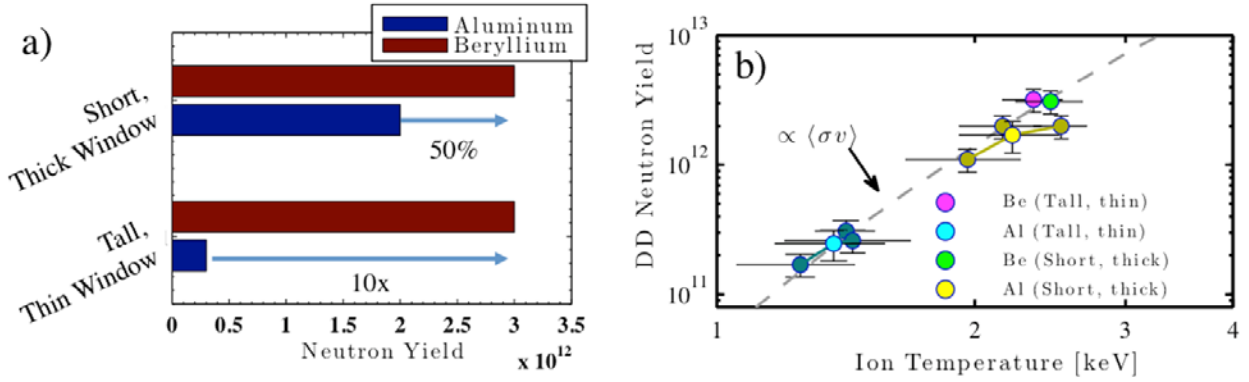

Figure 2.7. DD neutron yield and T_i illustrating improved MagLIF performance when Al cushions are replaced with Be cushions. (a) Measured DD neutron yield on two different classes of MagLIF implosions (7.5 mm tall, 3.4 µm thick window and 10 mm tall, 1.5 µm thick window). The blue bars are from implosions where Al cushions were used and the red bars from those where Be cushions were used. (b) Same data as a function of ion temperature T_i, indicating that both T_i and DD neutron yield are improved when Al is removed from the target.

2.3.3 Hypothesis #3 for degraded performance: Implosions deviate significantly from 1D

The structure of the stagnated plasma column could be significantly different from 1D and 2D pictures, which would result in reduced pressure, degraded confinement and lower DD neutron yield. This can be caused by hydrodynamic mix that evolves during stagnation, poor symmetry limiting compression, portions of the column being "pinched" off, resulting in inefficient conversion of implosion kinetic energy to thermal energy.

Evidence:

- X-ray images at stagnation reveal a column with helical structure and significant axial variations in intensity (Figure 2.8). The helical structure is reminiscent of the dominant helical structure of the Magnetic Rayleigh Taylor (MRT) instability on the outer surface of the liner. 3D GORGON simulations show that the helical column alone can account for ~30-50% reduction in neutron yield compared to 1D.
- In some axial locations, the radial emission profile is double peaked. 3D GORGON simulations, which produce this emission profile, suggest that this signature is characteristic of liner material bisecting the hotspot. This effect, when considered in conjunction with the helical stagnation column, can account for up to ~10× reduction in neutron yield, although this degradation is dependent on the degree of perturbation imposed in these calculations. Presently, these calculations impose a surface roughness in an effort to reproduce late time radiography rather than self-consistently evolve the instabilities.
- Some x-ray emission images reveal "breaks" in the column (Figure 2.9). These breaks in the emission can be caused by regions of enhanced liner ρR attenuating the hot-spot x-ray emission, reduced hot-spot density and/or temperature, or penetration of the liner into the hot spot at that location.

Additional Hypotheses:

- Cross-field thermal conduction is not captured adequately by the theories implemented in the design codes and as a result stagnation temperatures are overestimated.
- Magnetic flux compression is not as efficient as expected due to enhanced transport of the field from the hot spot to the liner, which can cause the hot spot to cool more rapidly than expected during stagnation.
- Asymmetric laser heating generates vorticity and enhanced scrape mix from the liner and limits compression.
- Axial mass-flux is larger than expected leading to enhanced losses of mass and energy during compression.

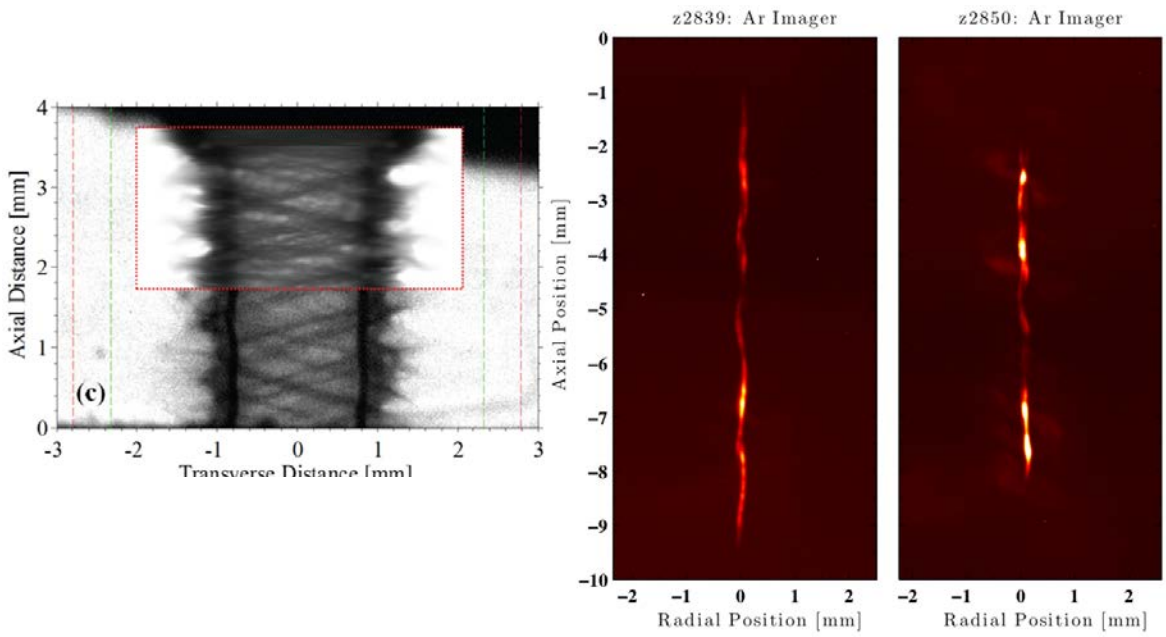

Figure 2.8. Left panel shows an experimental radiograph and 3D calculation (inset) illustrating the helical nature of the classical MRT instability when an axial field is imposed on the target. The two colored images to the right show monochromatic crystal images recorded on two MagLIF experiments. In these images it is evident that the stagnation column has an apparent helical structure, introducing a 3D effect that potentially could have an impact on the performance.

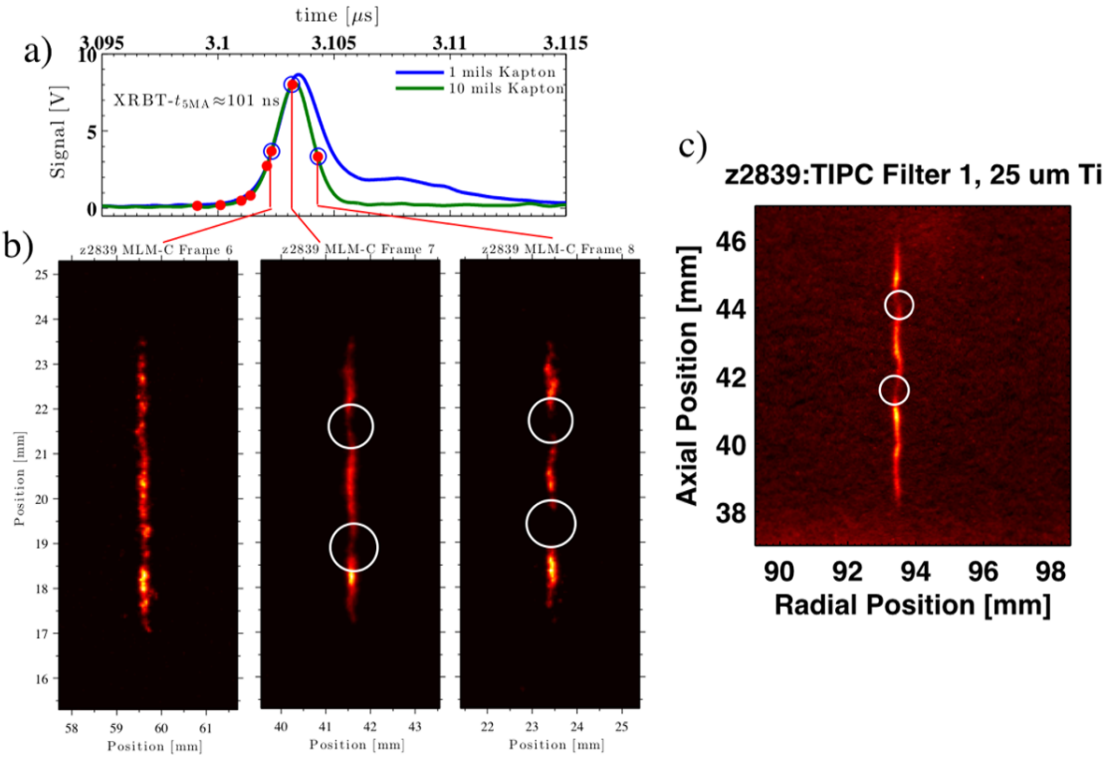

Figure 2.9. (a) X-ray pulse recorded on a MagLIF experiment. (b) Three time-resolved pinhole images of the same experiment showing the evolution of the column. By the peak x-ray power, two dim regions are apparent that become more pronounced as the x-ray pulse decays. (c) Time integrated, filtered pinhole images showing the same structure as in the time-resolved images.

2.4 New experiments, analysis-methods and diagnostics for studying current hypotheses

Experiments to address the laser coupling hypothesis:

- Development of a DPP laser heating platform.
    - Laser heating experiments are currently underway to empirically determine, with simulations as a guide, a laser configuration and "low mix" pulse shape that will lead to similar plasma conditions in successful MagLIF implosions that did not incorporate DPP. Once a suitable laser configuration and pulse shape have been determined, an integrated test will be performed at Z. This new platform is expected to be more understandable and predictable from laser heating point of view and constitute the basis for future experiments.
- Laser-only experiments to measure preheat energy coupled to the gas.
    - Understanding the amount of laser energy coupled to the gas is a bare minimum as far as initial conditions are concerned. The integrated performance is highly sensitive to this quantity, which will be studied under a variety of laser configurations in a dedicated campaign using ZBL instead of Z to hopefully make faster progress.
    - Laser-only experiments are also being performed at OMEGA-EP, OMEGA, and the NIF to characterize beam propagation, energy deposition, and laser induced mix as a function of initial density, laser power, and energy.
- In-situ measurements of the preheated fuel temperature as a function of time.
    - The plan is to image Ne emission (from doped fuel) looking down through the LEH window. Time and spectrally resolved emission will be recorded by the newly developed hybrid CMOS camera coupled to a spectrometer.
- Dependence of stagnation parameters on preheat energy coupled to the gas
    - Once the preheat conditions are understood and the amount of preheat energy deposited can be manipulated without significantly affecting the mix, it is essential to track the dependence of target performance on this quantity. This should be done with a number of different target and laser configurations. Simulations predict significant performance gains with higher energy coupled. However, this depends somewhat on how the energy is coupled and distributed. Furthermore, the energy coupled can affect how much B-field is retained in the hot spot, affecting the inhibition of thermal conductivity throughout the implosion.

Experiments to address the mix hypothesis:

- Evaluation of MagLIF liners with thickened ends to mitigate a potential source of laser induced mix in addition to mitigating the wall/electrode instability.
    - The wall/electrode instability can cause the material at both ends of the liner to race ahead and implode prematurely. Thus far, an annulus of material placed on the inside of the liner, i.e., the cushion, has been used as part of the target design to mitigate this instability. "Thick-end" liners have been demonstrated in separate radiography experiments to be equally effective. This design will eliminate a potential mix source in the MagLIF implosion and widen the laser entrance channel.

- Position dopants in the target to determine where and when mix is being generated in integrated experiments and how it is distributed in the hot spot at stagnation.
    - The first series of experiments in this campaign will be executed this summer. Due to the difficulties of diagnosing the preheated plasma directly, this is an attempt to unravel the source and transport of mix using integrated experiments. Detectable, but not detrimental, levels of cobalt will be placed on the inner surface of the liner or the cushions. At stagnation, Co should emit detectable levels of line radiation that will be measured with the XRS3 x-ray spectrometer. This instrument provides axial spatial resolution, which enables an understanding of how uniformly distributed the initially localized dopants are in the hot spot at stagnation. A series of experiments with the dopants in different locations and possibly with different laser configurations will provide crucial information to disentangle the mix problem.
- Development of a "low-mix" cryogenic MagLIF platform.
    - The target for this series is designed to minimize mix and maximize energy coupling. Mix mitigation features include: 400 nm LEH windows, increased separation distance between the initial window location and the imploding target region, thickened liner with no internal cushions, and a much larger beam bump (depth and diameter) at the bottom of the target.
- Exploration of so-called "mix mitigation" coatings (e.g. LiH or frozen D_2 coating on the inner surface of the target).
    - It is clear that mix is an issue, and that replacing Al fuel-facing components with Be significantly improves the performance. As such, the ability to fabricate composite liners using a thin Be outer shell surrounding a thicker LiH or LiD bulk is currently being pursued. In the future, it may be possible to use liquid or solid D_2 to achieve the same function. In the case of LiH, oxidation could be an issue that negates the positive impact of replacing the Be. If oxidation can be kept to an acceptably low level, a one-for-one replacement of Be mix with LiH mix is expected to provide enhanced performance.
- Understand the generation and transport of mixed material.
    - Once the laser energy deposition is characterized, it is critical to understand how the mixed material is generated during laser heating and how it is transported. Radiative losses are the dominant loss mechanism and non-fuel contaminants are by far the most significant contributors to the radiated power loss. The quantity and origin of these contaminants must be understood to mitigate this effect. For example, the recommended course of action would be different if the window contributes to the majority of the mix or if the cushions are the source. Simulations are required to understand this, but due to the nature of mix calculations, a significant body of data will be required to constrain them. As such, it is expected that this campaign to be carried out at a number of facilities, including OMEGA-EP and ZBL. Due to relatively low temperatures of the preheated plasma, conventional x-ray spectroscopy is extremely challenging to implement and use in these experiments. As few, if any, proven technologies exist to study this particular problem, new techniques must be employed to understand this issue. Likely candidates are optical scattering, x-ray scattering, x-ray fluorescence and visible/UV/XUV spectroscopy.

Experiments to address the 3D hypothesis:

- Exploration of MagLIF liners with increased and decreased initial aspect ratios (liner radius/liner width).
    - By measuring the changes in morphology at stagnation and changes in a variety of performance metrics (temperature, yield, pressure, etc.), we can begin to assess the importance of the observed 3D structures. 2D simulations generally predict that performance will degrade as the liner is made thicker. However, in 3D it is entirely possible that performance will improve with a thicker liner if the instabilities are worse than currently suspected by some. Measuring the properties of a stagnated plasma that is significantly more 1D than currently achieved will go a long way towards resolving the debate over the significance of the observed 3D structures.
- Stagnation radiography of surrogate targets.
    - Radiographing the dynamics of stagnation in a surrogate target allows for direct probing of the stagnation column and the evolution of the helical instability during deceleration and disassembly. This will bound the 3D nature of the stagnation column in integrated experiments, allowing a lower bound to be placed on the amount of degradation incurred from 3D effects. This platform will also allow us to assess the efficacy of various mitigation strategies such as thicker liners and coated liners.
- Integrated experiments with dielectric coatings.
    - A recent experiment has demonstrated that use of a dielectric coating to mitigate ETI growth produces a stagnation column that has significantly improved emission uniformity, but degraded performance. The cause of the degraded performance must be investigated and mitigation strategies must be tested. The structure of this stagnation column lends itself to analysis using effective 1D models improving confidence in our interpretation of the results, providing high value despite the degraded performance.

Experiments to address other hypotheses:

- Dependence of stagnation parameters on the initial B-field
    - Though not directly related to the three hypotheses given above, this is a fundamental aspect of the scaling of MagLIF [2.9]. Simulations universally predict improved performance with higher initial B-field. Currently, all experiments are performed with an initial field of 10 T, but a field of 30 T is expected to be achieved with existing technology, however, this will severely inhibit diagnostic access. As such, before this effort is taken up in earnest, a clear understanding of our stagnation conditions and preheat performance must be developed to allow good inferences in the absence of a full diagnostic suite.

New Diagnostics and Improvements:

- Neutron Imaging
- Burn History
- Time resolved T_e
- Higher resolution and higher photon energy imaging (time resolved)
- Higher precision yield measurements

- Radiographic capability on integrated experiments
- Laser energy coupling on integrated experiments
- Laser backscatter energy and angular distribution
- Radiated power measurements in-flight
- Improved characterization of existing nTOF detectors and their environments for higher precision and confidence in
    - Ion temperature measurements
    - Be areal density measurements
    - BR measurements
- 1D axial space-resolved nTOF detectors (for $T_i(z)$ and $r_{Be}R(z)$)

3. 'Stagnation' in Laser Direct Drive (LDD)

3.1 LDD concept

LDD implosion physics including fuel assembly and hot-spot formation are studied in spherically symmetric, direct-drive, DT-layered implosions [3.1, 3.2] at the 60-beam, 30-kJ, 351-nm OMEGA Laser System [3.3]. These implosions are hydrodynamically-scaled from ignition designs, where the radius of the capsule and laser pulse duration scale with the laser energy as $E_{\text{laser}}^{1/3}$, and the laser power scales as $E_{\text{laser}}^{2/3}$. The parameter space of calculated adiabat α [defined as the mass-averaged ratio of the fuel pressure to the Fermi-degenerate pressure P_{Fermi} in the dense imploding DT shell $\left(\alpha \equiv P/P_{\text{Fermi}}\right)$] and implosion velocity v_{imp} (the maximum mass-averaged velocity of the imploding shell) are explored for LDD implosions at OMEGA. Typical capsules consist of a plastic (CH) ablator enclosing a cryogenic DT layer (Figure 3.1). v_{imp} is varied by changing the thickness of the CH [7.5 to 12 μm] and/or DT layer [40 to 80 μm]. Pulse shapes have one to three pickets preceding the main pulse. Ignition requires $\alpha = 1.5 - 3$ corresponding to a Convergence Ratio (CR) > 22.

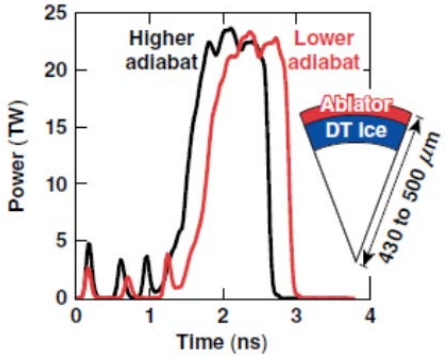

Figure 3.1. LDD implosion designs at OMEGA using a cryogenic DT capsule and different laser pulse shapes. The adiabat α is changed in the designs by varying the picket energies and timing. Laser energies on capsule are varied from 26 kJ to 29 kJ.

The hot spot pressure, P_{hs} and conversion efficiency of the laser energy into shell-kinetic energy and hot-spot thermal energy E_{hs} are critical parameters for ignition. P_{hs} scales [3.1] as $P_{\text{hs}} \sim P_{\text{abl}}^{1/3} v_{\text{imp}}^{10/3} / \alpha$, where P_{abl} is the ablation pressure. In the cross-beam energy transfer (CBET) process [3.4, 3.5, 3.6], non-absorbed light that is reflected/scattered from its critical surface or refracted from the under-dense plasma acts as an electromagnetic seed for the stimulated Brillouin scatter of incoming (incident) light [3.7]. For irradiation conditions appropriate for ignition capsule designs, CBET has been shown to reduce the capsule absorption and resulting P_{abl} of OMEGA direct-drive implosions by as much as 40% [3.4, 3.5, 3.6] and simulations indicate that as large as a 60% reduction of P_{abl} could occur in NIF-scale implosions [3.8]. In addition to CBET, hydrodynamic instabilities and low-mode drive asymmetries can reduce P_{hs} and generate mix of cold fuel/ablator into the hot spot impacting the implosion performance rate [3.9]; and supra-thermal electron generation by the two-plasmon–decay (TPD) instability and stimulated Raman scattering (SRS) [3.10], which can preheat the DT fuel, raise α and lower the hot-spot pressure for a given P_{abl} and v_{imp}. It is however, modeled at this point that supra-thermal electrons from TPD can utmost reduce areal densities by 10% and are not considered to be the dominant mechanism for the reduction in performance. SRS is not observed on OMEGA for the typical cryogenic implosions.

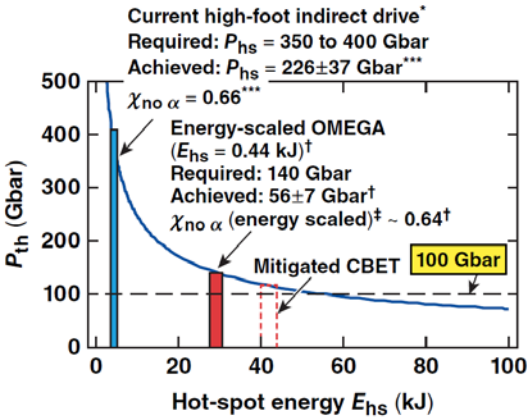

Figure 3.2. The ignition threshold pressure P_{th} as a function of the hot-spot energy E_{hs}. LID [3.11, 3.12, 3.13] and LDD implosion performance [3.2, 3.14] are highlighted. LDD needs a hot-spot pressure above 120 Gbar to achieve ignition. CBET reduces the efficiency of coupling the laser energy to the hot spot and decreases the predicted E_{hs} from 40 kJ to 30 kJ (corresponding to the energy-scaled OMEGA implosion achieving E_{hs} = 0.44 kJ without CBET mitigation) and raises P_{th} to 144 Gbar. The energy-scaled generalized Lawson criterion without alpha heating [3.13, 3.14, 3.15] for the OMEGA direct-drive DT cryogenic implosions $\chi_{no\ \alpha}$(energy scaled) [3.2, 3.14] is similar to the generalized Lawson criterion without alpha heating $\chi_{no\ \alpha}$ achieved with current indirect drive implosions on the National Ignition Facility [3.11, 3.12, 3.13].

Figure 3.2 illustrates the ignition threshold pressure $P_{th} = 250\ \text{Gbar}/\sqrt{E_{hs}/10\ \text{kJ}}$ as a function of the hot-spot thermal energy [3.1, 3.2]. Increasing laser coupling and E_{hs} reduces P_{hs} required for ignition. Symmetric direct-drive–ignition capsule designs at the NIF are predicted to couple up to 40 kJ to the hot spot, resulting in a required pressure of P_{hs} = 120 Gbar, as shown in Figure 3.2, which can be achieved in an implosion with a *CR* = 22, and in-flight aspect ratio (*IFAR*)—defined as the shell radius divided by its thickness at maximum implosion velocity—of 24 when the energy coupling losses from CBET have been mitigated. Current OMEGA implosions reach E_{hs} = 0.44 kJ without any CBET mitigation. When scaled to 1.8 MJ UV energy at the NIF with scaled CBET losses, these OMEGA implosions are predicted to reach $E_{hs} \approx$ 30 kJ, increasing the required P_{hs} to 144 Gbar (see Figure 3.2). With this E_{hs}, capsule designs with *CR* = 25 and an *IFAR* of 33 are required to reach the ignition conditions albeit with decreased robustness to hydrodynamic instabilities and low-mode drive asymmetries. Because of the required E_{hs} for direct-drive ICF, the ignition-relevant P_{hs} and *CR* are lower than the requirements for indirect-drive ICF: P_{hs} = 350-400 Gbar and *CR* = 30 to 40 [3.11]. An inferred P_{hs} of 226±37 Gbar has been reported for NIF indirect-drive ICF implosions [3.12], demonstrating that it is possible to compress DT to a pressure that exceeds the requirements for direct-drive ignition.

The highest hot-spot pressure achieved with direct-drive ICF cryogenic, layered DT implosions at OMEGA is P_{hs} = 56±7 Gbar [3.2]. The implosion had a calculated adiabat of 3.2. This is nearly half of the ignition-threshold of 120-150 Gbar for direct drive ICF scaled to NIF energies. 3D simulations suggest that low-mode distortion of the hot spot seeded by laser-drive non-uniformity and capsule-positioning error reduces the neutron rate and inferred P_{hs} [3.2, 3.9]. As discussed in the literature, a generalized Lawson criterion without alpha heating [3.13, 3.14] was calculated for each implosion and energy scaled [3.14, 3.15] from the OMEGA laser energy of 26 kJ to the maximum NIF laser energy of 1.9 MJ [3.2, 3.14]. The

measured ρR, measured neutron yield, and 1D calculated shocked DT mass at stagnation are used to evaluate the energy-scaled, generalized Lawson criterion without alpha heating (χ_{scaled}), which is shown in Figure 3.3 as a function of fuel adiabat. The blue symbols, red symbols, and orange line represent the experimental results, 1D simulations including CBET, and 1D simulations with CBET mitigated, respectively. These hydrodynamically-scaled OMEGA implosions achieved a χ_{scaled} of ~ 60% [3.2, 3.14], similar to indirect-drive [3.11, 3.12, 3.13]. Here P_{hs} and confinement time τ are estimated without accounting for alpha heating to assess the pure hydrodynamic performance of the implosion. The laser-plasma coupling is assumed to be the same for OMEGA and NIF; experiments at the NIF are ongoing to assess this assumption. As the adiabat is reduced from $\alpha = 6$, the experimental points (blue symbols in Figure 3.3) deviate from the 1-D simulations including CBET (red symbols in Figure 3.3). This behavior is attributed to the long wave length perturbations caused by laser drive non-uniformity and capsule offsets. The χ_{scaled} for the experimental points (blue symbols in Figure 3.3) peaks at α ~3.5 and then decreases with decreasing adiabat. This behavior is attributed to hydrodynamic instabilities seeded by short wavelength perturbations from microscopic surface debris and laser imprint affecting the implosion performance, in addition to the long-wavelength modes. Figure 3.3 shows that more-robust, higher-adiabat ignition designs could be considered if CBET were mitigated and long-wavelengths perturbations were reduced.

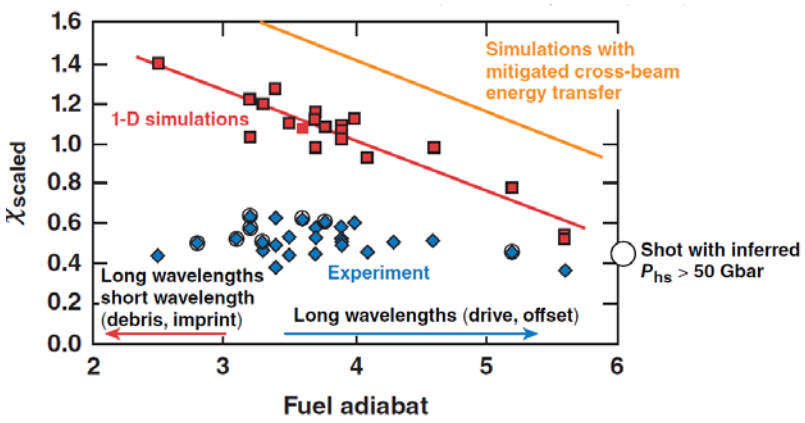

Figure 3.3. The energy-scaled, generalized Lawson criterion without alpha heating (χ_{scaled}) is plotted as a function of fuel adiabat. The blue symbols, red symbols, and orange line represent the experimental results, 1D simulations including CBET, and 1D simulations with CBET mitigated, respectively. The experimental points where the inferred P_{hs} > 50 Gbar are highlighted as circle symbols.

The 100 Gbar campaign is underway at OMEGA to understand the physics of assembling an ignition-relevant hot spot. Laser improvements are being made to drive a more uniform implosion and to mitigate CBET. The current method of filling the DT cryogenic capsules via permeation will be extended to a fill-tube capsule to accommodate non-permeable ablator materials used to mitigate laser imprint and laser plasma interactions [3.1]. The fill-tube capsules will have less microscopic surface debris and defects, and the quicker capsule fill time will lead to less radiation damage to the ablator, which will reduce the seeds for hydrodynamic instabilities. Enhancements in diagnostics with multiple lines of sight and new modeling and simulation capabilities have been initiated to understand 3D effects on implosion performance. Achieving 100 Gbar at OMEGA is a critical part of the National Direct-Drive Program (see Chapter 1) and will require a detailed scientific understanding of direct-drive physics.

3.2 Observations and physical picture of the stagnated fuel

Observations indicate that:

- Implosion performance, measured through the DT neutron yield and ρR, degrades with decreasing α.
- Apparent T_i, determined from neutron spectral widths, indicates increasing variation among the various diagnostic Line-Of-Sight (LOS) as CR is increased, suggesting a significant ion velocity distribution in the compressed core.
- Differences in apparent T_i from the DT and DD neutron spectra suggesting residual kinetic energy (RKE) during stagnation.
- Distortions are observed in the time-resolved x-rays images of the hot spot indicating long wavelength asymmetries.

Simulations are required in addition to these observations of late-time implosion properties to construct a picture of the compressed core. It is hypothesized that different mechanisms dominate the performance for high ($\alpha \gtrsim 3.5$) and low ($\alpha \lesssim 3.5$) adiabats. According to simulations, high-α implosions are relatively insensitive to short wavelength non-uniformities imposed by the single-beam non-uniformity of the laser (laser imprint). Long wavelength non-uniformities, seeded by beam imbalances, capsule roughness and offset are more likely responsible for the degraded implosion performance of the higher-α implosions. These asymmetries distort the core sufficiently to produce a bubble of hot plasma through which heat and DT fuel escape and thus degrade the implosion performance. Simulations also indicate that the performance of low-α implosions is dominated by short wavelength non-uniformity seeded by laser imprint. In these implosions, the compressed core has low a CR because of the reduced density of the inflight shell. Cold fuel and ablator material is also mixed into the fuel.

An important implosion-performance metric is the hot-spot pressure, P_{hs}, determined from x-ray and neutron data [3.2]. The total observed DT neutron yield is given by

$$Yield \approx \int_{\Delta t_{burn}} dt \int_{V_{hs}} n_D n_T \langle \sigma v \rangle dV \tag{3.1}$$

$$Yield \sim \underbrace{n_D n_T T_i^2}_{P_{hs}^2} \underbrace{\left(\int_{V_{hs}} \frac{\langle \sigma v \rangle}{T_i^2} dV \right)}_{\text{Depends on } T_i \text{ and } V_{hs}} \underbrace{\Delta t_{burn}}_{\text{Measured burn width}}, \tag{3.2}$$

where, n_D and n_T are the deuteron and triton number density, respectively, T_i is the ion temperature, V_{hs} is the-hot spot or burn volume, $<\sigma v>$ is the reactivity, and Δt_{burn} is the burn width. V_{hs} is inferred from x-ray images of the hot core [3.16]. T_i is inferred from the width of the neutron spectra using the approach outlined in ref. [3.17]. Δt_{burn} is determined from the measured neutron rate history [3.18]. These measurements are discussed in more detail later. The following observations are related to the inferred hot-spot pressure in OMEGA cryogenic implosions:

- The hot-spot pressure decreases with decreasing α or increasing CR. The ratio of the hot-spot pressure to simulated 1D pressure decreases for $CR > 18$, as shown in Figure 3.2.
- The highest hot-spot pressure achieved is 56±7 GBar [3.2]. In comparison, direct-drive hot-spot ignition requires a pressure of at least 120 GBar.

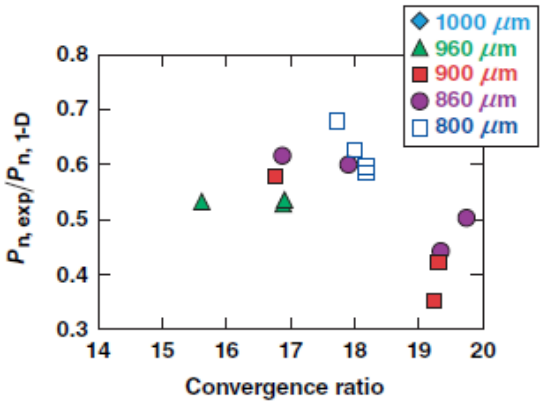

Figure 3.4. The ratio of the experimentally inferred hot-spot pressure to the simulated 1D pressure is shown as a function of calculated convergence ratio *CR*. The implosion performance drops for convergence ratio above 18. The different symbols correspond to different capsule outer diameter. Note that the highest ratio is obtained when the capsule radius is slightly smaller than the laser beam diameter of 825 μm, defined as the diameter encircling 95% of the laser energy.

Observations related to each of the components of the hot-spot pressure:

DT neutron yield: The absolute DT neutron yield decreases with decreasing adiabat α. The ratio of the measured yield, relative to the simulated 1D yield (Figure 3.5a) also decreases with decreasing α. The experimentally determined ρR, inferred from the down-scattered [3.19] and back scattered neutron spectra [3.20], also decreases with decreasing α (Figure 3.5b).

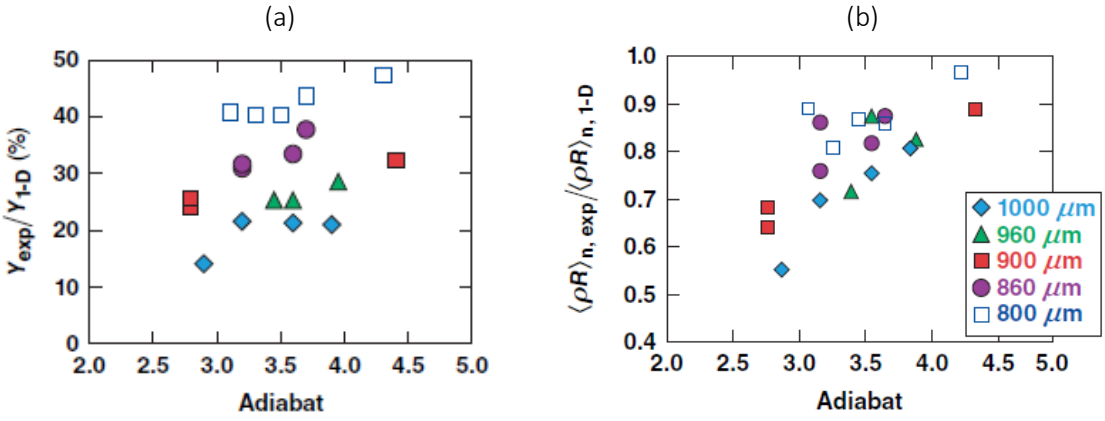

Figure 3.5. Implosion performance improves relative to 1D with increasing adiabat α. (a) The ratio of the experimental DT neutron yield to the simulated 1D yield as a function of calculated α. (b) The ratio of the experimentally inferred ρR to 1D burn-averaged (or neutron-averaged) ρR as a function of α.

Burn volume V_{hs}: The hot-spot radius R_{hs} at stagnation is inferred from the 4-8 keV x-ray image recorded with the 16-channel Kirkpatrick–Baez microscope, which provides 6-μm spatial resolution and 30-ps temporal resolution [3.16]. The 17% intensity contour radius R_{17} of the gated x-ray image is related to the R_{hs} based on 1D simulations as $R_{hs} = 1.06 \times R_{17}$. It is observed that this radius increases as α decreases, contrary to 1D simulations. The 4-8 keV x-ray energy range may not be the best surrogate to measure the neutron emission volume. Increasing the photon energy to greater than 12 keV for the x-ray image may measure a more representative neutron emission volume.

Apparent T_i is inferred from nTOF data along three LOS using the technique outlined in ref 3.17. These inferred values of T_i vary significantly depending on viewing angle around the implosion, and the variation increases with decreasing α and increasing CR (Figure 3.6). Simulations indicate that such variation in T_i is possible when RKE is substantial at peak burn. This large and increasing variation with decreasing α is suggestive of large-scale non-radial fuel flows caused by long wavelength perturbations. One source of such flow is the shot-time location of the cryogenic capsule, which is typically not at the center. However, no correlation between the T_i variation and magnitude of this offset has been observed.

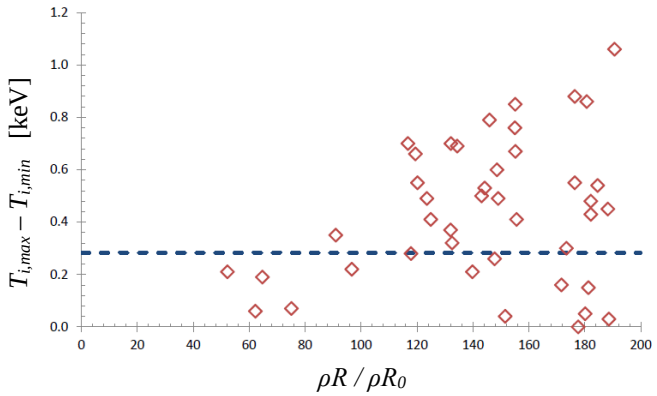

Figure 3.6. Variation in apparent T_i versus ρR (normalized to initial ρR_0). The apparent T_i is inferred from the width of the neutron spectrum. Each data point represents one implosion. A larger variation in T_i is observed with increasing ρR (and decreasing α and increasing CR).

Burn width is determined by fitting the measured neutron rate [3.18] with a Gaussian function, which has a temporal width (FWHM) equal to Δt_{burn}. The uncertainty in the measured burn width is ± 10%. As shown in Figure 3.7a, measured burn widths are typically truncated relative to 1D simulations. Simulations indicate that this truncation occurs when long wavelength perturbations from beam imbalances distort the hot spot and reduce the clean burn volume. This difference between simulations and measurements raises one source of correction of the simulated quantities because the simulated hot-spot pressure increases in time as CR increases (Figure 3.7b). If the measured DT neutron yield peaked earlier than the simulated, a lower hot-spot pressure sampled by the neutrons would be inferred. This is corrected for by using the measured neutron rate to sample the pressure and ρR in the simulation.

The ratio of the experimentally-inferred and 1D-simulated hot-spot pressure increases with increasing adiabat α when the measured neutron rate is used to sample the pressure (Figure 3.8a). Similarly, the ratio of the experimentally-inferred ρR and 1D-simulated also increases with increasing adiabat α (Figure 3.8b). It should also be noted that with decreasing α, the hot-spot pressure and ρR increasingly deviate from the simulated values.

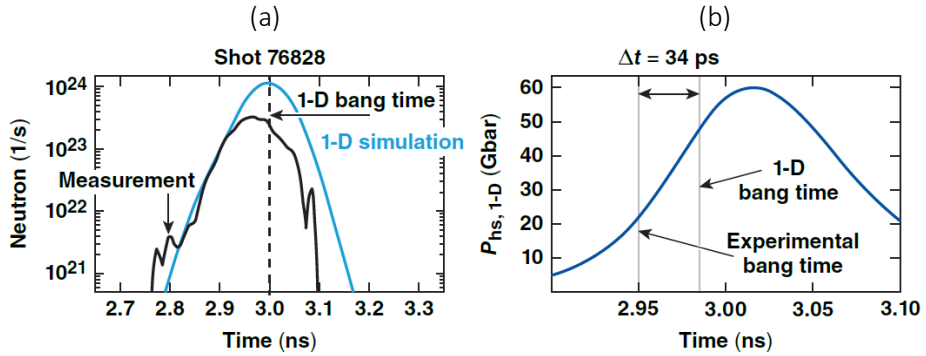

Figure 3.7. Implosion performance improves relative to 1D simulation with increasing adiabat α. (a) Measured neutron rate (black) compared to 1D simulated neutron rate (blue). (b) Simulated evolution of the hot-spot pressure versus time. The hot-spot pressure at the time of the 1D-simulated peak neutron production is larger than the pressure at the time of the measured peak neutron production.

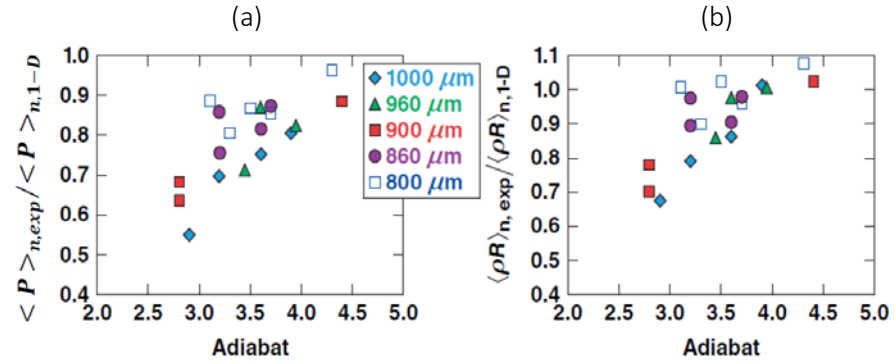

Figure 3.8. Implosion performance improves relative to 1D simulation as the adiabat α increases. (a) Ratio of the experimentally-inferred (from measured neutron rate) and 1D-simulated hot-spot pressure versus adiabat α. (b) Ratio of the experimentally-inferred and 1D-simulated ρR versus adiabat α.

3.3 Current state of modeling and simulation/data discrepancies

3.3.1 Hypothesis #1 for degraded performance: Errors in 1D simulations

It is possible that with decreasing α, design errors can lead to significant deviations between simulation and experiment. It is speculated that these errors can include:

- Mistimed shocks from pickets or shocks from the main pulse that are not modeled in simulation. Typical conditions in the shell during shock transit are $n_e \sim 10^{23}$ cm^{-3}, $T_e \sim 10$ eV, which corresponds to a plasma coupling parameter (Γ) of ~ 1. Material properties such as equation of state (EOS), and opacity are not well known under such moderate/weakly coupled conditions and such errors may contribute to shock mistiming.
- Errors in transport properties of the conduction zone: Typical electron densities in the conduction zone (the region between the ablation surface and laser deposition region) vary from 10^{23} cm^{-3} to 10^{22} cm^{-3} with T_e varying from 80 eV to ~1 keV during the main pulse in an OMEGA cryogenic implosion. Under these conditions, the material is partially ionized and its ionization properties and effects on heat conductivity coefficient are not well-known. Heat conduction primarily sets up the

ablation pressure to drive LDD capsules. Since $P_{hs} \sim P_{abl}^{1/3} V_{impl}^{10/3} \alpha^{-1}$ where P_{abl} is the ablation pressure, errors in heat conduction can result in incorrectly modeled hot spot pressure.

- Error in the inner-surface relaxation perhaps due to additional shocks, low-level preheat, or errors in calculating the sound speed resulting from uncertainties in material properties may potentially inject more material in the hot spot and reduce compression.

3.3.2 Hypothesis #2 for degraded performance: Long-wavelength non-uniformities in high-adiabat implosions

Asymmetries are observed in the gated x-ray images of the hot spot. The cold shell asymmetry is unknown thus far. Based on the hot-spot measurements alone, it is unclear if the observed asymmetry leads to a reduction in performance. Long-wavelength asymmetries are suggested by the apparent T_i measurements, which indicate the presence of significant RKE at peak compression.

3D simulations with the ASTER code [3.19] indicate that imbalances between beams (10 % power imbalance, 10 ps RMS beam mistiming, and 20 µm RMS beam mis-pointing) can potentially introduce long-wavelength asymmetries. These non-uniformity seeds cause truncation of the burn relative to spherically symmetric simulations (Figure 3.9a), and a bubble of hot gas that distort the cold shell (Figure 3.9b), increases the hot-spot volume, reduces DT neutron yield, and introduces ρR variations. The apparent T_i measured in different directions also vary significantly in these simulations, consistent with observations. It is thus hypothesized that long wavelength modes from beam imbalances can result in the observations characteristic of high-α implosions.

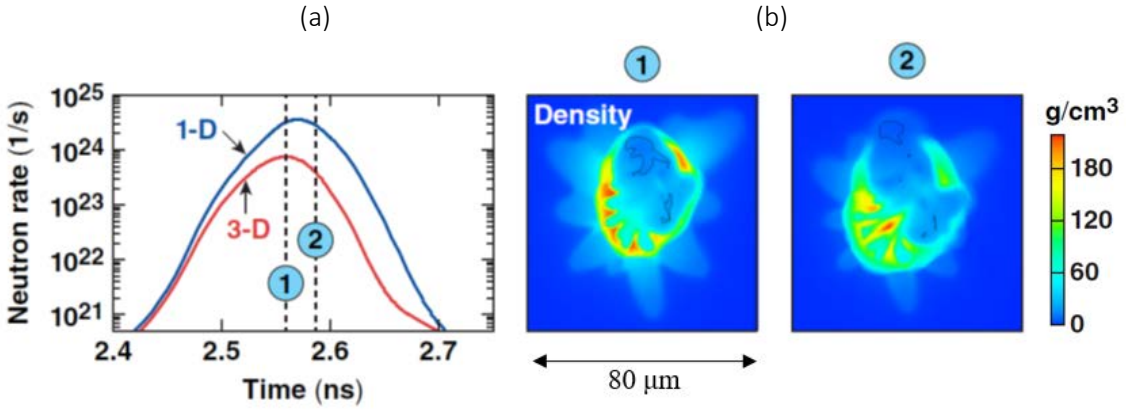

Figure 3.9. Simulated picture of the compressed hot spot and shell. (a) Simulated neutron rate without perturbations (blue) and with long-wavelength perturbations from beam imbalance (red). (b) Mass density profiles as viewed from the equator in 3D simulations that include beam imbalance (see text). The numbering corresponds to the times indicated in (a).

3.3.3 Hypothesis #3 for degraded performance: Effect of stalk and glue resulting in mix

Spherically symmetric simulations, which do not include the effect of ablator carbon in the hot spot, have shown that the ratio of the hot-spot x-ray emission to $Y_n^{0.57}$, where Y_n is the DT neutron yield, should be approximately one [3.21]. Significantly higher values of this ratio would suggest materials other than D or T in the hot spot. Relatively thick-ablator-layer implosions (where the CH thickness $\gtrsim$ 8 µm) indicate increasing values of this ratio with decreasing α (Figure 3.10.) The increased observed emission from the

hot spot is highly suggestive of mix from the ablator. For thinner values of CH ablators, all the carbon is ablated and none remains to be injected into the hot spot.

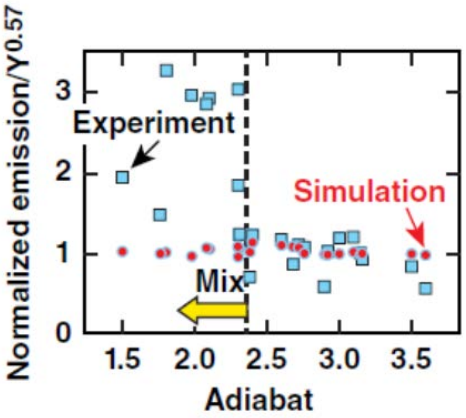

Figure 3.10. Indication of increased fuel-ablator mix as the adiabat α is decreasing. Red data points show 1D-simulated yield-normalized x-ray emission. The experimental data for the cryogenic DT implosions are shown by the blue boxes. Each point represents one implosion at OMEGA.

3D ASTER simulations suggest that jets of cold material can be injected into the hot spot due to the stalk or the glue that attaches the stalk to the capsule (Figure 3.11a). This may be responsible for the increasing mix observed in the experiments. When beam imbalance alone is included in the simulation (without a stalk), the perturbation from the stalk that launches a jet is not evident. (Figure 3.11b).

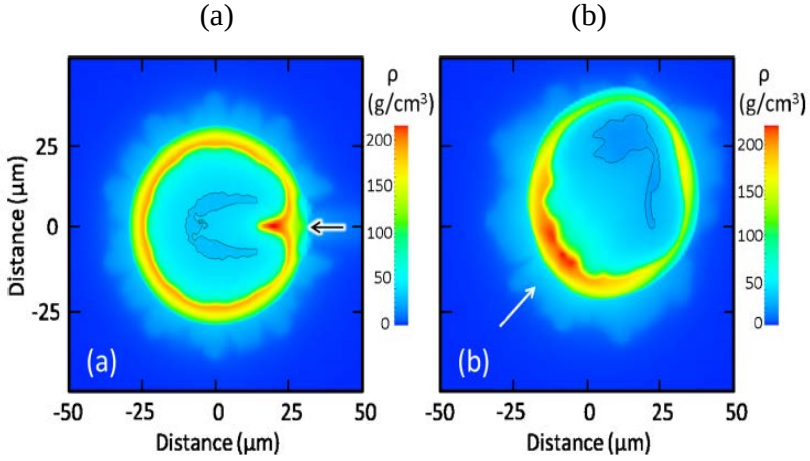

Figure 3.11. Jets of cold material either from the ablator or the shell may be responsible for the increasing mix observed in the experiments. (a) Mass density contours from a 3D ASTER simulation, viewed from the equator, showing the effect of the stalk (black arrow) and beam geometry. (b) Including the effects of beam imbalances alone (no stalk). The offset direction, shown by the white arrow, corresponds to a 10 μm offset.

3.3.4 Hypothesis #4 for degraded performance: Effect of laser imprint for low-adiabat implosions

Laser imprint from single beam non-uniformity can potentially compromise the implosion performance. DRACO [3.22] simulations that include the effect of imprint and related short wavelength growth indicate that the average shell density in α = 2.5 implosions is reduced, resulting in an ineffective piston (Figure 12a) [3.23]. These simulations also indicate a reduced DT neutron yield relative to the spherically symmetric simulation (Figure 12b), reduced ρR, increased hot-spot size, and reduced hot-spot pressure. It is surmised that the higher-α implosions ($\alpha \gtrsim 3.5$) are relatively sensitive to imprint while lower-α implosions are most likely affected by this mechanism.

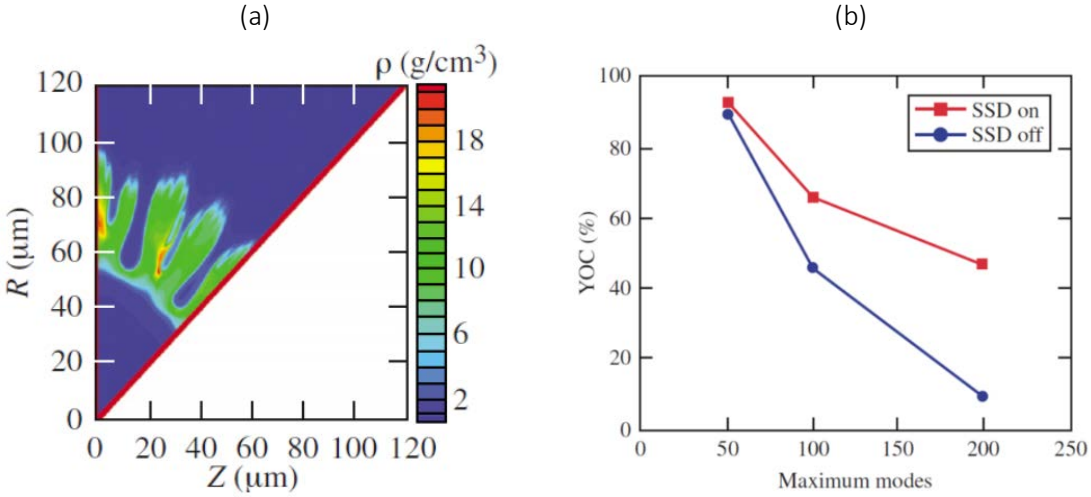

Figure 3.12. (a) Mass density contour from a 2D DRACO simulation including the effect of laser imprint for an α = 2.5 implosion. (b) The ratio of the DT neutron yield from simulations with imprint to the DT neutron yield from a 1D simulation. The SSD on case has less laser imprint than the SSD off case.

3.4 Path forward

3.4.1 1D physics-related science campaigns

Characterize in-flight density relaxation

Ongoing planar foil experiments are used to determine the relaxation of the inner surface from radiography and emission from mid-Z tracers located in the inner surface. The results from these experiments will be used to identify if the experimentally inferred location of the inner surface is different from simulation and if this mechanism can explain observations of reduced ρR in low-α implosions.

High precision shock timing

The VISAR diagnostic [3.24] will be used to set the shock timing in cryogenic capsule implosions [3.25]. These experiments will be used to study shock timing in liquid DT-filled CH capsules of thickness 7.8-8 μm, which are relevant for ongoing cryogenic capsule implosions, and to study shock catch-up and velocity from the main pulse. Some differences in the velocity of the shock from the main pulse were observed previously. Experiments to further address this difference are ongoing.

3.4.2 Very high adiabat, 1D cryogenic campaign

Spherically symmetric simulations are typically used to define the 1D nature of an implosion. To date, no ablatively driven implosions at OMEGA have been deemed "1D-like"; non-uniformities have to be invoked to explain the observations. With increasing α, it is to be expected that the performance will be less compromised by non-uniformities. Observations of stagnation properties in very high adiabat ($\alpha \gtrsim 6$) implosions are being used to construct a self-consistent picture of the compressed core based entirely on measured quantities. The goal of this campaign is to find an adiabat α above which it can be concluded that the implosion is spherically symmetric, independent of simulations. This implosion would serve as a touchstone. Trends in various implosion-relevant quantities such as implosion velocity, α, imprint, fuel-composition will be studied. The predicted trends will be used to understand and quantify degradation mechanisms. This in turn, could serve to identify where improvements in experimental/engineering parameters are required to improve performance.

3.4.3 Precision power balance/beam pointing/offset campaign

A precision power balance campaign has been initiated at OMEGA to improve the laser power imbalance between beams during the pickets and main pulse. The goal with this campaign is to obtain an on-capsule drive intensity non-uniformity level of 1% RMS averaged over 100 ps. A better understanding of the laser drive non-uniformity and an assessment of the necessary improvements at OMEGA, including the laser and laser diagnostics, is expected by the end of FY17. Based on simulations, it is expected that this campaign should improve performance of the $\alpha \gtrsim 3.5$ implosions.

3.4.4 Mix cryogenic implosion campaign with Ge-doped ablator

Cryogenic DT implosions with Ge-doped CH ablators are being studied to identify the extent of hydrodynamic mixing of ablator material into the compressed fuel layer and hot spot [3.26] using time-integrated, spatially-resolved x-ray spectroscopy. The laser drive ablates most of the ~8-μm thick CH ablator, which is doped with trace amounts of Ge (~0.5% atomic) and surrounds the cryogenic DT fuel layer. A small fraction of the CH-ablator material is mixed into the compressed shell and hot spot by the ablation front Rayleigh-Taylor hydrodynamic instability seeded by laser imprint [3.23], the capsule mounting stalk, and surface debris [3.27]. The dependence of mixing on the implosion adiabat ($2 < \alpha < 7$) will be measured and compared to hydrodynamic simulations. Results from this campaign will identify the extent of mix and whether it can be a source for the observed performance degradation.

3.4.5 High-Z overcoats for imprint mitigation

The use of a thin (~50 nm thickness) Au overcoat on the surface of the ablator of a direct-drive implosion capsule has improved the measured performance [3.28], which is likely due to reduced laser imprint [3.29, 3.30]. Reduced imprint relative to undoped CH ablators has also been measured in focused (cone-in-shell) imprint experiments where CH ablators are doped with mid-Z materials like Si and Ge [3.31, 3.32]. X-ray radiography campaigns are in progress on OMEGA, OMEGA EP, and Nike to discriminate the laser imprint reduction effect from any increase in the adiabat caused by an increase in x-ray preheat from the Au layer blow-off in the coronal plasma.

3.4.6 Diagnostic development

In support of the cryogenic program the following diagnostics will be developed:

- 3D gated, x-ray imaging of the hot-spot: Image the hot-spot x-ray emission along three orthogonal lines of sight with temporal resolution in the 10-30 ps range and spatial resolution of ~ 5 μm.
- 3D gated, x-ray imaging of the in-flight shell: Image the coronal plasma soft x-ray emission to diagnose low-mode non-uniformities in the laser drive on capsule along six lines of sight.
- Time-resolved, spectrally-resolved measurement of x-ray continuum from the hot spot to infer the spatially-averaged T_e and compare with the apparent T_i inferred from nTOF diagnostics.
- Gated UV imager to diagnose scattered light from CBET.
- A full-beam path, full-energy ultraviolet equivalent target plane detector to measure the far-field fluence distribution on capsule,
- Install a 2nd and 3rd shielded nTOF on OMEGA: The compressed ρR is inferred from the down-scattered primary DT neutrons, and is currently diagnosed using a shielded nTOF detector [3.20] and the magnetic recoil spectrometer (MRS) [3.19]. In addition, the nTOF measures the DD-n and DT-n yields and the apparent T_i inferred from the DD-n and DT-n spectra along a single LOS. A second and third shielded nTOF will be added to diagnose spatial variations in the areal density of the compressed DT, fluid flow along the direction of the detector from the inferred DD-n and DT-n T_i, and RKE in the hot spot from the variation of the apparent T_i along the multiple diagnostic LOS.

3.4.7 Cross-beam-energy-transfer (CBET) mitigation

As described in Section 3.1, CBET reduces the ablation pressure by as much as 40% for OMEGA implosions resulting in a reduction in the implosion velocity by as much as ~10% [3.4, 3.5, 3.6]. This affects the hot-spot pressure: $P_{hs} \sim P_{abl}^{1/3} V_{impl}^{10/3} \alpha^{-1}$, where the ablation pressure P_{abl} is determined by the laser energy deposited in the corona and heat conduction to the ablation surface. CBET mitigation is needed to achieve 100 Gbar on OMEGA. Improved implosion velocity has been demonstrated in OMEGA experiments by CBET mitigation with decreasing ratio of the laser spot size to the capsule diameter [3.6]. However, these have been achieved at the expense of increased non-uniformity. Simulations have been used to design several approaches to mitigate CBET at OMEGA while not significantly compromising the laser drive non-uniformity on capsule. Since CBET is a late-time phenomenon during the laser drive, smaller beam sizes than the capsule size that reduce late time crossing of the laser rays are being considered. A two-state beam zooming scheme has been proposed [3.33] to achieve an initial laser spot size that corresponds to the capsule radius and a spot size smaller than the capsule radius later in time to reduce ray crossings. Another approach being considered is to use different wavelengths on neighboring beams and reduce the extent of CBET by moving the resonance region of CBET in the corona, similar to that implemented in LID [3.34]. CBET mitigation is an important research effort for LDD.

4. 'Stagnation' in Laser Indirect Drive (LID)

4.1 Introduction

Over seventy five cryogenic DT implosions have been performed at the NIF, spanning a number of capsule and hohlraum designs and laser pulse shapes (see Figure 4.1). This chapter focuses on the high-foot design [4.1], since it is the highest performing design to date, and the most studied. Most high-foot implosions (CH HF) were performed in a standard size Au or DU hohlraum with a high-gas-fill density (1.6 mg/cm^3). Two experiments tested, an adiabat-shaped variant of the high-foot pulse (CH HF AS) in the same hohlraum, demonstrating higher fuel compression as predicted. More recent experiments have transitioned to testing a larger size low-gas-fill hohlraum (CH HF LGF), which exhibits significantly reduced levels of LPI.

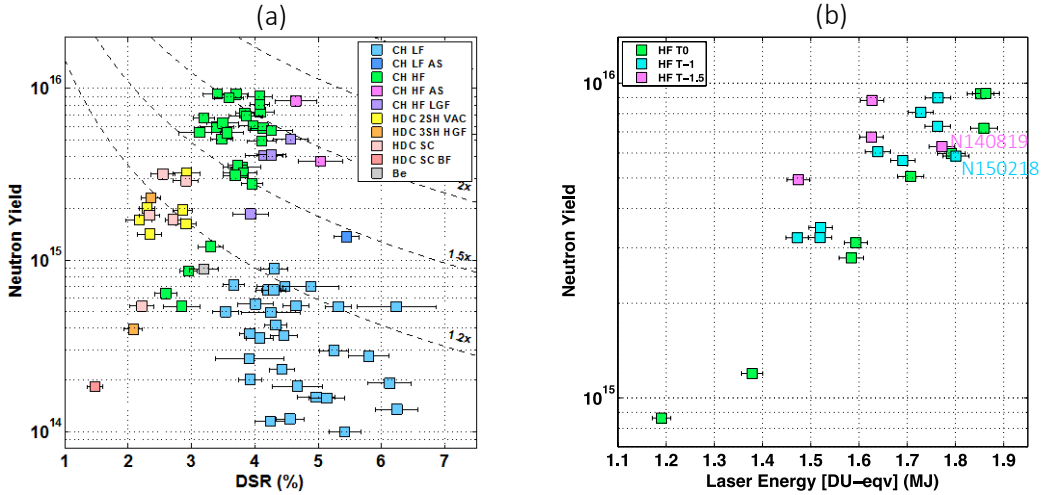

Figure 4.1. (a) Yield vs. DSR for all cryogenic DT implosions. The dashed curves indicate the yield enhancement due to alpha heating. (b) Yield vs. Laser Energy for the CH HF campaign, with data separated by ablator thickness (T0 = 195µm, T-1 = 175µm, T-1.5 = 165µm). The horizontal axis represents the laser energy that corresponds to a DU hohlraum—for a DU hohlraum this is the actual delivered laser energy; for a Au hohlraum this is the delivered laser energy derated by 6.5% to correct for the difference in drive efficiencies and obtain the laser energy that would be required if the experiment were performed in a DU hohlraum.

The CH HF campaign can be divided into three sub-campaigns, which used progressively reduced capsule-ablator thickness ranging from 195µm (T0), to 175µm (T-1), and then to 165µm (T-1.5). In each sub-campaign, the laser energy was progressively increased by increasing either the peak power or pulse duration, until either the maximum permissible energy of NIF, or a "performance cliff", was reached. As seen in Figure 4.1b the neutron yield Y_n responded in a systematic way, in general, to the increases in laser energy and reductions in ablator thickness—both of which have a principal effect of increasing the capsule implosion velocity. Two implosions appear to have fallen off the observed scaling with laser energy, N150218 and N140819. These implosions were driven with the highest laser energies, respectively, in the T-1 and T-1.5 series. A key question for guiding the experimental campaign is do we understand the performance and degradation mechanisms of the experiments to date. Within the context of the NISP working group, this question is addressed by examining our level of understanding of the state of the assembled fuel at stagnation.

4.2 Physical picture of the stagnated fuel and ablator

The time-evolution of the implosion is characterized through a substantial set of experiments with both surrogate (re-emits, keyholes, 2D ConAs, and Symcaps) and cryogenically-layered DT capsules. Key observations from these experiments are described here.

4.2.1 Implosion asymmetry

There is strong experimental evidence of implosion asymmetry arising from at least two sources: time-dependent radiation drive asymmetry, and engineering features (the capsule support tent and possibly the fill-tube) [4.2].

Drive asymmetry — an early-time P2 drive asymmetry in the foot of the pulse is observed in keyhole data showing a shock break out at the equator that is up to ~300 ps earlier than at the pole. The P2 asymmetry persists in in-flight 2D ConA experiments showing a positive P2 (prolate) shell at a convergence ratio of 4–5×. Time-resolved 2D x-ray self-emission images typically show a negative P2 (oblate) and negatively swinging (-dP2/dt) hot-spot shape around bang time (time of peak neutron production). The in-flight radiography measurements also show a P4 asymmetry in the shell, which is an inherent to the hohlraum geometry and beam pointing scheme employed in the high-foot experiments. Additionally, some variable degree of M4 asymmetry in the x-ray self-emission images is observed from pole. In some cases a large P2 asymmetry is accompanied by a hole, or absence of emission, at the center of the hot spot as viewed from the pole (see Figure 4.2).

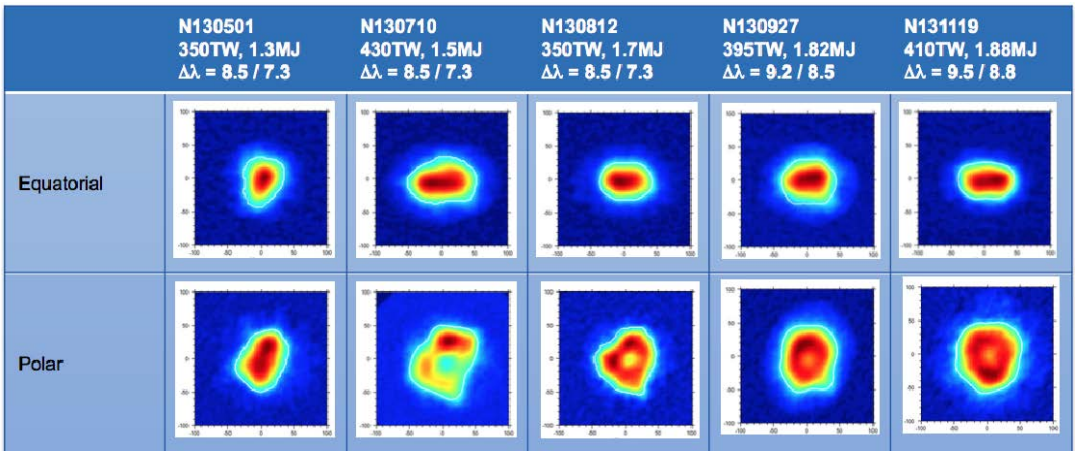

Figure 4.2. X-ray self-emission images observed on the equator and pole for a set of high-foot implosions with T0 ablator and increasing laser energy.

Engineering features — evidence of the capsule support tent seeding ρR perturbations can be seen in ablator density reconstructions from 2D ConA radiographs, albeit at a ~3× lower level than observed in the low-foot experiments [4.3]. For most high-foot implosions, effects of the tent are not distinguishable in x-ray self-emission at stagnation—except for the highest velocity, thinnest ablator (T-1.5) implosions, which show "pinching" of the hot spot at the poles, suggestive of tent perturbation. The other major engineering feature, the fill-tube, is not directly observed in the high-foot implosions. However, it is very prominent in the self-emission in symmetrically-driven HDC implosions, which suggests that it may be present in high-foot implosions but masked by the other asymmetries present in the system.

Cold fuel asymmetry — strong anisotropy of the cold fuel is inferred from both flange-nuclear-activation-detector (FNAD) measurements [4.4] and neutron-spectrometry measurements using nTOFs and the Magnetic Recoil Spectrometer (MRS) [4.5, 4.6]. From the neutron-spectrometry measurements of the yield ratio between down-scattered and primary neutrons (DSR), a directional fuel ρR is inferred. Complementary insights into the spatial distribution of the cold fuel is obtained from the FNADs data. The FNADs measure the relative and directional yield of unscattered primary neutrons at nineteen locations around the implosion (the unscattered yield is high where the cold fuel is thin and vice versa), and the data often show angular variations consistent with low-mode ρR asymmetries. On approximately 50% of the high-foot implosions, the FNADs data are fit with spherical harmonic distributions with modal content up to L=2, which generally show regions of high ρR at the poles (see example in Figure 4.3a). The other 50% of the data show residual RMS deviation from the L=2 fit, implying the existence of L-modal content > 2. Models of the hot spot and cold fuel with only simple low-mode shape distortions struggle to predict this excess RMS at modes L>2. In this context, it should be noted that this interpretation of equivalency between directional unscattered neutrons and ρR is only valid for a quasi-spherical hot-spot surrounded by a dense shell. In the case of toroidal hot spots, the variation in FNADs data may be low despite the existence of high ρR poles. In the "tent-less" implosions, a high ρR feature was observed close to the fill-tube axis suggesting that at least in the case of a 30 µm fill tube the impact on the shell symmetry is significant (an example of a possible ρR perturbation due the fill tube is shown in Figure 4.3b). In addition, a new analysis method has been developed to isolate an image of the cold fuel by using the primary image to compensate for the flux from the hot spot [4.7]. Preliminary analysis show regions of higher cold fuel mass at the poles for implosion N150422, consistent with inferences of the FNADs data shown in Figure 4.3a.

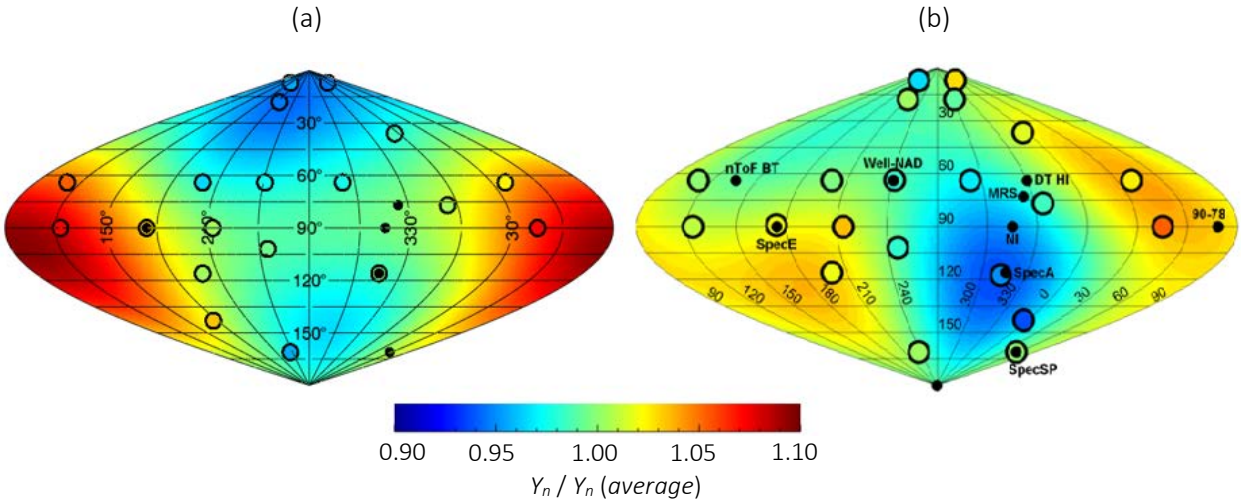

Figure 4.3. Y_n/Y_n(average) ratio measured with the FNADs (positions indicated by the open circles) for (a) implosion N150422 and (b) implosion N160628. Smaller black data points indicate the positions of the nTOFs and the MRS used for the DSR measurements, from which a directional ρR is determined. The color map was generated by fitting a low-order spherical harmonics to the data. The data shown in (a) illustrate high ρR values at the poles, while the data in (b) show a high ρR feature at the location of the fill tube. This mass perturbation and associated radiation shadowing may be seeding a large defect that could perturb the stagnated high-density shell. A Y_n/Y_n(average) variation of about ±10% roughly corresponds to a ρR asymmetry of about ±500 mg/cm^2.

4.2.2 Hot-spot temperature anomalies

The apparent burn-averaged T_i (DT T_i and DD T_i) are obtained from measurements of the spectral widths of the DT and DD neutron peaks, as recorded by nTOF detectors. These two measurements are expected to differ by ~5% since, due to the differences in reactivities, they have different weightings over the temperature distribution of the hot spot. Figure 4.4a shows that for shots where DT T_i is <4 keV, the DT T_i and DD T_i are self-consistent, but as DT T_i increases >4 keV the two measurements increasingly diverge. At the highest temperatures, a DT T_i of ~5.5 keV and DD T_i of ~4.7 keV, or a differential of ΔT_i ~ 0.8 keV, are measured and compared to an expected ΔT_i of ~0.3 keV. In both cases, these measurements are 0.5–1 keV higher than expected from theory or simulations for implosions with those yields [4.2].

The width of the neutron spectrum is affected by both the thermal T_i and residual flow velocities in the hot spot. Thus, and discussed for the other approaches, the true thermal T_i may be lower than the measured apparent T_i if large bulk-flow velocities or RKE are present in the implosion during burn. An isotropic (radial) velocity field would contribute equally in all directions, whereas a non-isotropic field would result in differences in the apparent T_i values recorded along different LOS. Figure 4.4b shows the observed LOS isotropy for all DT implosions. Relatively little variation is observed across the five individual measurements of DT T_i or DD T_i with different LOS, indicating no strong evidence for large anisotropic flows in the hot-spot (but strong isotropic flows can still be present) [4.8].

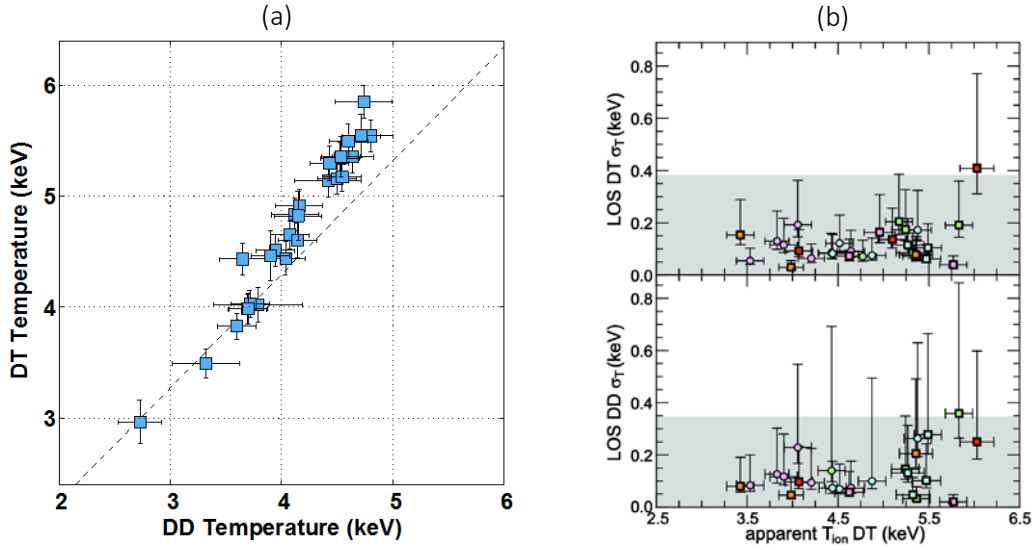

Figure 4.4. (a) Apparent DT T_i vs. DD T_i for the high-foot implosions. The dashed line is a fit to a simulation database that shows the predicted offset between the DT and DD T_i resulting primarily from the differences in reactivity. (b) DT T_i and DD T_i isotropy as a function of apparent DT T_i (ref. (4.8]). The observed LOS isotropy is calculated as the RMS variation of the individual nTOF detector measurements. The vertical error bars represent the 68% confidence interval; the gray bands represent the estimated systematic uncertainty.

4.2.3 Hot-spot mix

Mix of ablator material into the hot spot is diagnosed by three methods: line spectroscopy, continuum spectroscopy, and x-ray imaging. The first method [4.9] is based on x-ray emission measurements of Ge K-shell lines from the imploding Ge-doped capsules. It was used in low-foot implosions where Ge He-α line emission was routinely detected and used to infer a mix mass of 10's to 1000's ng of CH(Si:Ge) in the hot spot. It has been employed on one high-foot implosion in which no Ge He-α line emission was observed, providing an upper limit of a few 10's ng of ablator mix based on the detection threshold of the measurement. The second method [4.10] uses the ratio of the absolute x-ray continuum emission over the neutron emission to detect excess radiation produced by high-Z ablator material mixed in to the hot spot. The absolute x-ray emission from the implosion is measured at a photon energy of 10.85 keV with the south-pole-bang-time (SPBT) diagnostic. This method can be employed for all implosions since it does not rely on measurements of tracer materials added to the ablator, but directly measures emission from the ablator material itself. However, it is less sensitive than the line method, with a minimum detection threshold of ~100-150 ng of CH(Si) ablator mix. Figure 4.5 shows the observed x-ray-to-neutron-emission ratio for three implosion designs and indicates that no observable ablator mix has yet been detected above the detection threshold in high-foot experiments. The third method of temporally and spatially resolved x-ray imaging of the hot spot can reveal small bright features that are likely to be associated with ablator mix associated with the fill-tube, tent, or capsule defects. While such features have been observed in recent lower convergence HDC implosions they are not clearly observed in high-foot implosions. This does not necessarily mean that such features are not present, but they are difficult to isolate due to other structures in the hot spot.

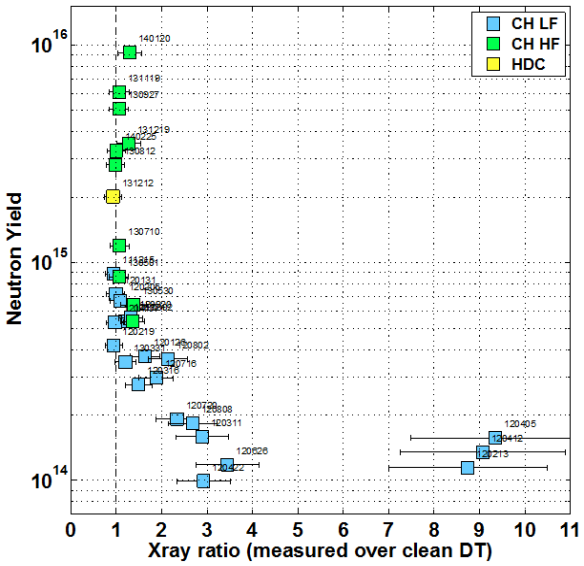

Figure 4.5. Neutron yield vs. x-ray-to-neutron-emission ratio for CH low-foot (CH LF), CH high-foot (CH HF), and HDC implosions. An x-ray-to-neutron yield ratio of 1 represents the expected ratio for a clean DT hot-spot with no ablator mix.

4.2.4 Burn width

The x-ray burn width is measured with the SPIDER streak camera diagnostic [4.11], and the nuclear burn width is measured with the GRH diagnostic [4.12], which probes the gamma rays from DT reactions. In Figure 4.6, both measurements show a general trend of decreasing burn width with increasing yield. However, the trend is more pronounced for x-rays which reaches a minimum burn width of ~110 ps, compared to ~135 ps for the gammas. From theory and simulations, the expectation is that these burn widths are similar, with a $\Delta t \lesssim 10$ ps.

4.2.5 Hot-spot pressure

A burn-averaged hot-spot pressure is inferred using a 1D isobaric model of the hot spot constrained by the experimentally measured Y_n, burn-averaged T_i, x-ray and neutron emission radii, and burn width. Figure 4.7 shows the inferred pressure versus coast-time. The coast-time is the defined as the time between the end of the laser pulse and bang time. As the laser energy or peak power was increased in the high-foot series, the coast-time decreased reflecting higher implosion velocities and the maintenance of ablation pressure for longer periods of time. In these experiments, a strong scaling of increasing stagnation pressure with reduced coast-time was osberved. However, the two implosions with the shortest coast-times, N150218 and N140819, show a drop in pressure (and a corresponding drop in Y_n), suggesting an apparent implosion-performance "cliff" was reached.

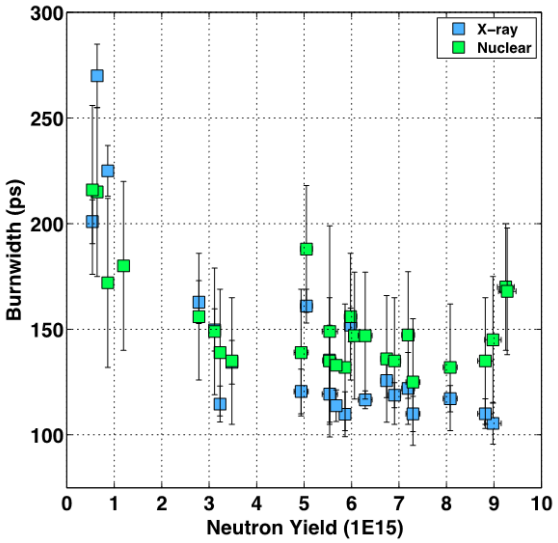

Figure 4.6. Measured x-ray and nuclear burn widths as a function of neutron yield Y_n for all high-foot implosions. For most implosions with yields >3×10^{15}, the burn widths are relatively constant, with x-ray widths of ~110 ps and nuclear widths of ~135 ps.

4.3 Experiment vs. Simulation

Post-shot simulations of the experiments can be either integrated hohlraum or capsule-only simulations. Integrated hohlraum simulations model the full interaction of the laser with the hohlraum and capsule. Capsule-only simulations use a frequency-dependent radiation drive generated from an integrated hohlraum simulation to model only the capsule implosion with higher resolution and fidelity than is possible in the full hohlraum simulation. Figure 4.8 shows the simulated 1D and 2D yields from integrated hohlraum calculations [4.13]. To match the implosion trajectories and in-flight and hot-spot shape from re-emit, keyhole, and ConA experiments requires multipliers on the drive and a model for the time-dependent CBET. The same set of drive multipliers are applied to all tuning and DT implosions. The agreement between the 2D simulations and experiment is fairly good, with

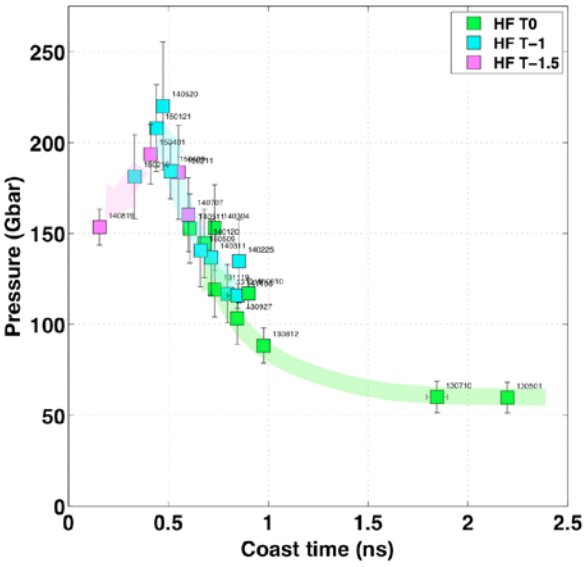

Figure 4.7. Inferred stagnation pressure vs. coast time shows strong scaling with decreasing coast-time, with an apparent performance "cliff" at ~220 Gbar.

experimental yield-over-simulated (YOS) mostly in the range of 40-100%. Of the other metrics, the X-ray P0 is matched for most implosions within a few microns, T_i, DSR and burn width are quite well matched for the lowest velocity implosions. However, as the velocity increases above 340 km/s the experiments exhibit higher apparent T_i, lower DSR and longer burn widths, than the simulations. In 1D the YOS is ~50% for the lowest velocity implosion at 300 km/s, but then falls with increasing velocity. At the highest velocities of ~375 km/s the implosions are predicted to ignite in 1D. The difference between the 1D and 2D shows the magnitude of the degradation due to low-mode drive asymmetry (these simulations do not include capsule surface roughness or engineering features).

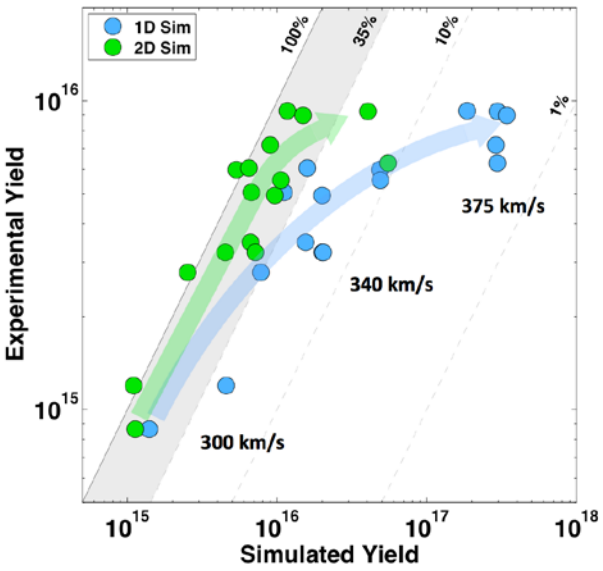

Figure 4.8. Measured Y_n vs. 1D and 2D integrated hohlraum simulations for high-foot shot series. The YOC for the 2D simulations is 40-100% for most implosions. In 1D, the simulations diverge from the experiments as the velocity increases, predicting the highest-velocity implosions at ~375 km/s to ignite.

Highly resolved 3D capsule-only simulations include all known perturbations, including the measured metrology of the capsule surface and ice, the support tent, and the fill-tube. Figure 4.9 shows simulated images of the hot-spot and dense shell at stagnation from 3D simulations of N130927 (195 µm ablator thickness, 350 km/s peak velocity), and N140819 (165 µm ablator thickness, 390 km/s peak velocity) [4.14]. In N130927, the low-mode drive asymmetry is predicted to be the dominant degradation mechanism, followed by the tent perturbation. In N140819—the thinnest shell, highest velocity implosion in the high-foot campaign—one clearly observes the effect of the stronger ablation-front instability growth at the fuel-ablator interface, larger tent and fill-tube perturbations. For both implosions, the 3D simulated Y_n, DSR and X-ray P0 values agree relatively well with the experimental data. However, they under-predict the apparent T_i by 0.5–1 keV, and under-predict the burn widths by ~40 ps. A caveat here is that the simulated T_i and DSR values are instantaneous post-processed values at bang time rather than time-averaged over the burn. This is due to the scale of the 3D simulations, which currently prevents running HYDRA with its inline Monte-Carlo neutronics package.

4.4 Current state of modeling and simulation/data discrepancies

A number of hypotheses have been formulated for explaining the experimental observables and identifying the sources for performance degradation relative to expectation and detailed post-shot simulation.

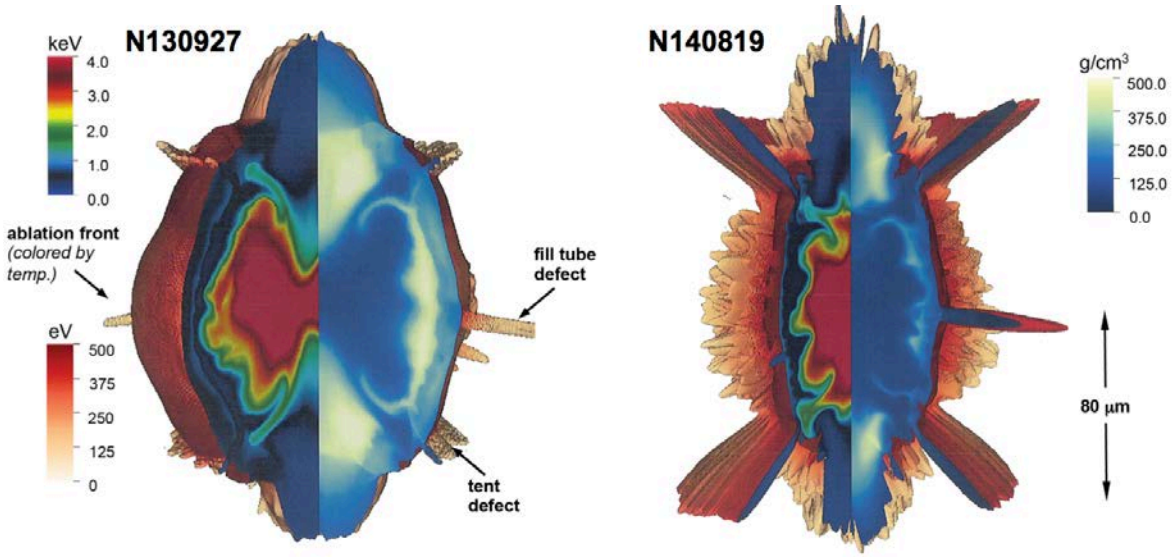

Figure 4.9. Density and temperature maps of DT hot spot and dense shell at time of peak neutron production from highly resolved 3D simulations of N130927 (195 µm ablator, 350 km/s), and N140819 (165 µm ablator, 390 km/s).

4.4.1 Hypothesis #1 – Radiation drive asymmetry is a principal degradation mechanism

Keyhole and 2D ConA implosions provide direct experimental evidence of early time and in-flight implosion-shape asymmetry that can very likely be attributed to radiation drive asymmetry. The limited accuracy of our physics models for high-gas-fill hohlraums restricts our ability to accurately predict the radiation flux asymmetry on the capsule from initial laser and capsule parameters. Post-shot simulations that are tuned to best match the observables suggest that radiation drive asymmetry is the dominant source of yield degradation, and that its impact increases significantly with increasing implosion velocity.

4.4.2 Hypothesis #2 – Tent is a significant degradation mechanism at high-implosion velocities

Diagnosis of in-flight 2D ConA implosions reveal a relatively small, though non-zero, ρR perturbation arising from the capsule support tent. There appears to be evidence of "pinching" of the hot spot induced by the tent in x-ray self-imaging of implosion N140819, the thinnest ablator, highest-velocity implosion. A 3D simulation of this implosion predicts significant growth of the tent perturbation and localized thinning of the shell at stagnation, suggesting that the implosion is on the verge of shell break-up and loss of confinement.

4.4.3 Hypothesis #3 – Fill-tube may be affecting hot-spot and shell symmetry

Time-resolved x-ray self-emission measurements sometimes show features that might be attributable to mix originating from the fill-tube, though the measurements are not conclusive. Measurements of the continuum radiation loss suggest that any such level of mix does not significantly enhance the radiation loss, but it may affect both the hot-spot shape and shell ρR uniformity. There are indications of these effects in more symmetrically driven HDC implosions. Recent HGR experiments also show evidence of the fill tube seeding a much larger perturbation than currently predicted in simulations.

4.4.4 Hypothesis #4 – Oxygen non-uniformities may be a source of instability growth

Internal inhomogeneity in the oxygen content in CH ablators will generate density and opacity modulations that are a seed for hydrodynamic instability growth. Recent simulations and work on capsule characterization indicate that a level of non-uniformity could be present in the capsules that would result in perturbations several times larger than the expected growth from surface roughness. However, sufficiently accurate measurements of the oxygen modulation in the ablator do not yet exist to reach a definite conclusion [4.15].

4.4.5 Hypothesis #5 – Hot electron preheat may be the cause of low DSR

Two VISAR observables have been identified as possible signatures of hot electron preheat in high-gas-fill hohlraums. These are (i) an acceleration of the 1st shock just prior to be overtaken by the 2nd shock, and (ii) premature blanking of the VISAR signal. Neither signature is seen in low-gas-fill hohlraums, which have 1-to-2 orders of magnitude lower levels of hot electron production as measured by FFLEX. The precise impact on implosion performance is uncertain, however, given the uncertainties in deriving the incident electron flux at the capsule from the FFLEX measurement.

4.4.6 Hypothesis #6 – Apparent T_i anomalies explained by residual flow velocities

The leading hypothesis for explaining the observed apparent T_i anomalies is that residual flow velocities in the hot spot lead to significant broadening of the DT and DD primary-neutron spectra, and that the true neutron-averaged thermal T_i values are substantially lower than the measured apparent T_i. There are two difficulties with this hypothesis: (i) if the true thermal T_i of the best performing implosions are closer to the expected DT T_i of 4 – 4.5 keV (from theory and simulations), then from straightforward kinematics theory, ΔT = DT T_i – DD T_i is expected to increase, but not close to the level of ΔT~0.8 keV observed experimentally; and (ii) a stronger apparent T_i anisotropy between the nTOF measurements might be expected to be seen. One way that these observations might be reconciled is if the differential scattering of DD vs. DT neutrons in the high-density shell strongly influences the probed DT and DD regions of the hot spot.

4.4.7 Hypothesis #7 – High apparent T_i explained by over-predicted thermal conductivity

Another hypothesis is that current simulations over-predict the hot-spot thermal conductivity. This could be due to self-generated magnetic fields, kinetic plasma effects, or possibly other effects not currently included in simulations. The motivation for this hypothesis is in fact that simulations, where the DT thermal conductivity is artificially reduced, show significantly better agreement with the observed yield, T_i and DSR.

4.4.8 Hypothesis #8 – Poorly known isotope concentration

There could be significant consequences if the actual D:T ratio of the ice differed from the requested 50:50 ratio. The measured DD to DT yield ratio is generally larger than expected from reactivity and scattering differences and would be more consistent with a D:T ratio of between 50:50 and 60:40, which has forced a re-examination of the isotopic composition of the fuel and associated uncertainties.

4.4.9 Hypothesis #9 – Impact of kinetic effects is more significant than expected

A number of kinetic or multi-component-fluid effects that could potentially affect the implosion behavior have been proposed. These include ion-species separation at the ablator-ice and ice-gas interfaces that could alter the local ion-species concentrations, spatially and temporally, within the hot spot and dense fuel. This could have a significant effect on relative DT and DD yields and neutron-averaged T_i values.

4.5 Proposed experiments, analysis and measurements

Proposed experiments, analysis, and measurements are listed in prioritized order.

Proposed Experiments:

- The most direct manner to test the different hypotheses for sources of performance degradation is to reduce or remove them. For hypothesis #1 (radiation drive asymmetry) this has been attempted with a very limited number of implosions, primarily using DT implosions. Given our current understanding it is possible that the early-time symmetry could be improved through additional keyhole and 2D ConA experiments and then assess the impact on performance in a cryogenically-layered DT-capsule implosion experiment. To assess this proposal one could evaluate the number of additional experiments likely to be needed to obtain a significant improvement in performance (stagnation quality or yield) and thereby test the hypothesis. [new]
- A different approach to testing #1 is to modify the design to move toward a regime where we expect to have better control of radiation drive asymmetry. This is currently being done in the CH HF LGF (CH high-foot low-gas-fill) design, which uses a lower gas-fill-density (0.6 g/cm^3) in a larger hohlraum (672) to simultaneously reduce LPI effects and increase the capsule drive uniformity. [in progress]
- Hypothesis #2 is being tested by developing alternative methods for supporting the capsule in the hohlraum and measuring the effect on the in-flight ρR modulation through x-ray backlighting experiments, and on the stagnation quality and yield through integrated implosion experiments. [in progress]
- Hypothesis #3 is being tested by developing alternative fill-tubes (such as smaller diameter fill-tubes) and measuring the x-ray self-emission feature of the fill-tube jet at stagnation using the near-symmetrically driven subscale HDC platform. [in progress]
- Repeat implosion N140819. The capsule used in this experiment was compromised by a "melt feature" or localized wrinkle in the shell that resulted in a radial distortion of ~2 μm. Repeating this implosion with a good quality capsule would clarify whether or not this feature was partially responsible for the observed performance degradation. [new]
- Achieve a quasi 1D (symmetrically-driven) DT implosion and use it to test degradation hypotheses and code predictions. For example, test effects of applied P1, P2, P4 mode asymmetries, roughened capsule surface, etc. [in-progress/new]

Proposed Analysis:

- The coupled effect of residual flow velocities and scattering on the measured DT T_i and DD T_i (#6) can be examined in 3D simulations with various levels of applied perturbations. [in progress]
- The development of a fast approximate time-dependent 3D implosion model would enable the exploration of a larger parameter space and facilitate the use of statistical methods to find configurations of the stagnated fuel that are consistent with various observations, such as the hot spot and cold fuel shape (#1), and the T_i anisotropy (#6). [in progress]
- A detailed analysis of the x-ray and nuclear burn histories may provide insight into the temporal evolution of the hot spot, and help to determine if differences between the two measurements are due to real physical effects or to instrumental uncertainties. [new]

Proposed Measurements:

- Extension of the 2D ConA x-ray backlighting platform to higher photon energies (>15 keV) would provide valuable information on the shape and ρR of the shell closer to stagnation where the effects of drive asymmetry and engineering defects would be amplified. The new crystal backlight imager (CBI) is the most promising diagnostic for this measurement. [in progress]
- A high accuracy measurement of the x-ray continuum slope could be used to infer an emissivity-weighted T_e for comparison with the neutron-averaged apparent T_i. An upgraded differentially filtered imager (Ross pair II) has been fielded recently and may be able to provide this data on future cryogenically-layered DT implosions. [in progress]
- Replacing the 2D pinhole imaging system on DIXI with a penumbral imaging system will improve the spatial resolution from ~10 μm to ~5-6 μm, enabling smaller-scale features in the hot spot to be resolved. It will also increase throughput, which will allow for harder filtering and imaging of the hot-spot at higher, optically thin, photon energies. [in progress]
- Increasing number of FNADs from 19 to ~50 would enable the relative fuel ρR distribution at stagnation to be resolved up to mode L=4, compared to the current limit of L=2. [in progress]
- Compton radiography to measure shape and ρR distribution of the shell. [in progress]
- A fast time-resolved electron T_e (<20 ps) could provide valuable information on the temporal dynamics and evolution of the hot spot. The existing SPIDER diagnostic could be optimized for a T_e measurement. An assessment of the expected measurement accuracy would be needed to proceed. [new]
- Improved characterization of oxygen modulation levels in CH capsules. [in progress]
- Implement a new Gas Cherenkov Detector, GCD3, to improve sensitivity and temporal response of gamma reaction history measurement. [in progress]
- Implement a time-resolved MRS (MRSt) to obtain simultaneous measurements of time-resolved neutron rate, apparent T_i, residual flow velocities, and fuel areal density [4.16]. [in progress]

5. Differences/Commonalities in some observed signatures in MDD, LDD and LID

Contrasting differences and commonalities in certain signatures observed in MDD, LDD and LID can be very instructive, illuminating and perhaps provide additional insights and ideas for new experiments and analyses that will advance our understanding of the physical picture of the stagnation process and state for the different approaches. This section aims to achieve that by providing a few examples of differences and some commonalities. A discussion of what these differences and commonalities could possibly mean is also touched upon. As a follow up to this discussion, more focused workshops will be held in FY17 to scrutinize and provide a deeper assessment of a particular topic (such as the ones described below).

5.1 Differences in observed signatures

- Significant differences in the neutron-measured T_i are observed in the different approaches. In MDD, the consensus is that the neutron-measured T_i represents a thermal temperature, while in LDD and LID it represents an apparent temperature that is strongly affected by bulk-fluid motion in addition to thermal temperature. The current working hypothesis for this observation is that the difference is driven by different implosion velocities and implosion stability (MDD vs LDD/LID). It is also notable that the observed apparent T_i varies strongly with LOS in LDD, while it is quasi-isotropic in LID. The hypothesis for this observation is that engineering features and drive asymmetries have a different impact on the observed apparent T_i. In the case of LDD, laser-drive asymmetries and stalk holding the capsule could possibly generate low-mode asymmetries and a single jet that generates non-isotropic apparent T_i. In contrast, the instabilities seeded by the tent and fill tube, in addition to the low-mode drive asymmetries, could possibly generate several jets predominantly in the radial direction and thus generate quasi-isotropic apparent T_i. The next NISP workshop in FY17 will focus on this topic.

5.2 Commonalities in observed signatures

- Observations suggest that the fill tube (LID), stalk (LDD) and cushions/LEH window (MDD) have an impact on the stagnation process and state. There is some evidence that the fill tube (or the glue attaching the fill tube to the capsule) in LID is generating a jet that mixes cold material into the hot spot and distorts both the hot-spot shape and surrounding high-density shell. A similar issue seems to exist in LDD, where a single stalk-induced jet could mix cold material into the hot spot, and thus be responsible for both elevated mix and distortions of the high-density shell. In MDD, a possibly related mechanism at the LEH window and cushions could introduce higher-Z material into the hot spot and distort it as well. As this issue is connected to the T_i issue discussed above, it should be a topic in an upcoming NISP workshop.

- Similarities in the shape of secondary DT-neutron spectra measured in different directions are observed in MDD and LID D_2 gas-filled experiments. Although not discussed in detail in this document for all approaches, the detailed shape of the secondary DT-neutron spectra observed in different directions provide information about the temperature and density asymmetries in the hot spot and the transport of DD-tritons. The shape of the secondary DT-neutron spectrum is also the key BR diagnostic in MDD (Figure 2.3), but additional insights could perhaps be gained by evaluating and contrasting these observations in an upcoming NISP workshop.

References

Chapter 1

[1.1] "2016 Inertial Confinement Fusion Program Framework", National Nuclear Security Administration, DOE/NA-0044, May (2016).

[1.2] S. A. Slutz *et al.*, "Pulsed-power-driven cylindrical liner implosions of laser preheated fuel magnetized with an axial field", Phys. Plasmas 17, 056303 (2010).

[1.3] V. N. Goncharov *et al.*, "Improving the hot-spot pressure and demonstrating ignition hydrodynamic equivalence in cryogenic deuterium–tritium implosions on OMEGA", Phys. Plasmas 21, 056315 (2014).

[1.4] M. J. Edwards *et al.*, "Progress towards ignition on the National Ignition Facility", Phys. Plasmas 20, 070501 (2013).

Chapter 2

[2.1] S. A. Slutz and R. A. Vesey, "High-Gain Magnetized Inertial Fusion", Phys. Rev. Lett. 108, 025003 (2012).

[2.2] M. R. Gomez *et al.*, "Demonstration of thermonuclear conditions in magnetized liner inertial fusion experiments", Phys. Plasmas, 22, 056306 (2015).

[2.3] S. B. Hansen *et al.*, "Diagnosing magnetized liner inertial fusion experiments on Z," Phys. Plasmas, 22, 056313 (2015).

[2.4] P. F. Knapp *et al.*, "Effects of magnetization on fusion product trapping and secondary neutron spectra," Phys. Plasmas, 22, 056312 (2015).

[2.5] P. F. Schmit *et al.*, "Understanding Fuel Magnetization and Mix Using Secondary Nuclear Reactions in Magneto-Inertial Fusion", Phys. Rev. Lett. 113, 155004 (2014).

[2.6] A. B. Sefkow *et al.*, "Design of magnetized liner inertial fusion experiments using the Z facility," Phys. Plasmas, 21, 072711 (2014).

[2.7] M. Geissel *et al.*, "Nonlinear laser-plasma interaction in magnetized liner inertial fusion" presented at the SPIE LASE, 9731, 97310O (2016).

[2.8] A. J. Harvey-Thompson *et al.*, "Diagnosing laser-preheated magnetized plasmas relevant to magnetized liner inertial fusion," Phys. Plasmas, 22, 122708 (2015).

[2.9] S. A. Slutz *et al.*, "Scaling magnetized liner inertial fusion on Z and future pulsed-power accelerators," Phys. Plasmas, 23, 022702 (2016).

Chapter 3

[3.1] V. N. Goncharov *et al.*, "Improving the hot-spot pressure and demonstrating ignition hydrodynamic equivalence in cryogenic deuterium–tritium implosions on OMEGA", Phys. Plasmas 21, 056315 (2014).

[3.2] S. P. Regan *et al.*, "Demonstration of fuel hot-spot pressure in excess of 50 Gbar for direct-drive, layered deuterium–tritium implosions on OMEGA", Phys. Rev. Letters 117, 025001 (2016).

[3.3] T. R. Boehly et al., "Initial performance results of the OMEGA laser system," Opt. Commun. 133, 495 (1997).

[3.4] I. V. Igumenshchev *et al.*, "Crossed-beam energy transfer in implosion experiments on OMEGA", Phys. Plasmas 17, 122708 (2010).

[3.5] I. V. Igumenshchev *et al.*, "Crossed-beam energy transfer in direct-drive implosions", Phys. Plasmas 19, 056314 (2012).

[3.6] D. H. Froula *et al.*, "Increasing Hydrodynamic Efficiency by Reducing Cross-Beam Energy Transfer in Direct-Drive-Implosion Experiments", Phys. Rev. Lett. 108, 125003 (2012).

[3.7] C. J. Randall and J. R. Albritton, Phys. Fluids **24**, 1474 (1981).

[3.8] P. B. Radha et al., "Direct drive: Simulations and results from the National Ignition Facility," Phys. Plasmas 23, 056305 (2016).

[3.9] I. Igumenshchev *et al.*, "Three-dimensional modeling of direct-drive cryogenic implosions on OMEGA", Phys. Plasmas 23, 052702 (2016).

[3.10] W. L. Kruer, in *The Physics of Laser Plasma Interactions*, Frontiers in Physics, Vol. 73, edited by D. Pines (Addison-Wesley, Redwood City, CA, 1988).

[3.11] O. A. Hurricane *et al.*, "Fuel gain exceeding unity in an inertially confined fusion implosion," Nature 506, 343 (2014).

[3.12] T. Döppner *et al.*, "Demonstration of High Performance in Layered Deuterium-Tritium Capsule Implosions in Uranium Hohlraums at the National Ignition Facility," Phys. Rev. Lett. 115, 055001 (2015).

[3.13] R. Betti et al., "Alpha Heating and Burning Plasmas in Inertial Confinement Fusion," Phys. Rev. Lett. 114, 255003 (2015).

[3.14] A. Bose et al., "Core conditions for alpha heating attained in direct-drive inertial confinement fusion," Phys. Rev. E 94, 011201(R) (2016).

[3.15] R. Nora *et al.*, "Theory of hydro-equivalent ignition for inertial fusion and its applications to OMEGA and the National Ignition Facility," Phys. Plasmas **21**, 056316 (2014).

[3.16] F. J. Marshall *et al.,* "Compact Kirkpatrick–Baez microscope mirrors for imaging laser-plasma x-ray emission", Rev. Sci. Instrum. 83, 10E518 (2012).

[3.17] T. J. Murphy *et al.*, "Interpretation of neutron time-of-flight signals from current-mode detectors", Rev. Sci. Instrum. 68, 610 (1997).

[3.18] C. Stoeckl *et al.*, "Neutron temporal diagnostic for high-yield deuterium–tritium cryogenic implosions on OMEGA," Rev. Sci. Instrum. **87**, 053501 (2016).

[3.19] J. A. Frenje *et al.*, "Probing high areal-density cryogenic deuterium-tritium implosions using downscattered neutron spectra measured by the magnetic recoil spectrometer", Phys. Plasmas 17, 056311 (2010).

[3.20] C. J. Forrest *et al.*, "High-resolution spectroscopy used to measure inertial confinement fusion neutron spectra on Omega", Rev. Sci. Instrum. 83, 10D919 (2012).

[3.21] T. C. Sangster *et al.,* "Improving cryogenic deuterium–tritium implosion performance on OMEGA", Phys. Plasmas 20, 056317 (2013).

[3.22] P. B. Radha *et al.,* "Multidimensional analysis of direct-drive, plastic-shell implosions on OMEGA ", Phys. Plasmas 12, 056307 (2005).

[3.23] S. X. Hu *et al.,* "Two-dimensional simulations of the neutron yield in cryogenic deuterium-tritium implosions on OMEGA ", Phys. Plasmas 17, 102706 (2010).

[3.24] P. M. Celliers *et al.,* "Line-imaging velocimeter for shock diagnostics at the OMEGA laser facility", Rev. Sci. Instrum. 75, 4916 (2004).

[3.25] T. R. Boehly *et al.,* "Multiple spherically converging shock waves," Phys. Plasmas 18, 092706 (2011).

[3.26] S. P. Regan *et al.,* "Hot-Spot Mix in Ignition-Scale Inertial Confinement Fusion Targets," Phys. Rev. Lett. 111, 045001 (2013).

[3.27] Igumenshchev *et al.,* "Effects of local defect growth in direct-drive cryogenic implosions on OMEGA," Phys. Plasmas 20, 082703 (2013).

[3.28] A. N. Mostovych *et al.,* "Enhanced Direct-Drive Implosions with Thin High-*Z* Ablation Layers," Phys. Rev. Lett. 100, 075002 (2008).

[3.29] S. P. Obenschain *et al.,* "Effects of thin high-Z layers on the hydrodynamics of laser-accelerated plastic targets ", Phys. Plasmas 9, 2234 (2002).

[3.30] M. Karasik *et al.,* "Suppression of Laser Nonuniformity Imprinting Using a Thin High-*Z* Coating," Phys. Rev. Lett. 114, 085001 (2015).

[3.31] S. X. Hu *et al.,* "Mitigating Laser Imprint in Direct-Drive Inertial Confinement Fusion Implosions with High-Z Dopants", Phys. Rev. Lett. 108, 195003 (2012).

[3.32] G. Fiksel *et al.,* "Experimental reduction of laser imprinting and Rayleigh–Taylor growth in spherically compressed, medium-Z-doped plastic targets", Phys. Plasmas 19, 062704 (2012).

[3.33] D. H. Froula *et al.,* "Mitigation of cross-beam energy transfer: Implication of two-state focal zooming on OMEGA", Phys. Plasmas 20, 082704 (2013).

[3.34] P. Michel *et al.,* "Energy transfer between laser beams crossing in ignition hohlraums", Phys. Plasmas 16, 042702 (2009).

Chapter 4

[4.1] O. A. Hurricane *et al*., "The high-foot implosion campaign on the National Ignition Facility", Phys. Plasmas 21, 056314 (2014).

[4.2] O. A. Hurricane *et al*., "Inertially confined fusion plasmas dominated by alpha-particle self-heating", Nature Phys., page 1, 11 April 2016.

[4.3] J. Lindl *et al.*, "Review of the National Ignition Campaign 2009-2012", Phys. Plasmas 21, 020501 (2014).

[4.4] C. B. Yeamans *et al.*, "Enhanced NIF neutron activation diagnostics", Rev. Sci. Instrum. 83, 10D315 (2012).

[4.5] M. G. Johnson *et al.*, "Neutron spectrometry—An essential tool for diagnosing implosions at the National Ignition Facility", Rev. Sci. Instrum.83, 10D308 (2012).

[4.6] J. A. Frenje *et al.*, "Diagnosing implosion performance at the National Ignition Facility (NIF) by means of neutron spectrometry", Nucl. Fusion 53, 043014 (2013).

[4.7] D. T. Casey *et al.*, "Fluence-Compensated Down-scattered Neutron Imaging using the Neutron Imaging System at the National Ignition Facility", Rev. Sci. Instrum. 87 11E715 (2016).

[4.8] M. G. Johnson *et al.*, "Indications of flow near maximum compression in layered DT implosions at the National Ignition Facility". Phys. Rev. E 94, 021202(R) (2016).

[4.9] S. P. Regan *et al., "*Hot-Spot Mix in Ignition-Scale Inertial Confinement Fusion Targets", Phys. Rev. Lett. 111, 045001 (2013).

[4.10] T. Ma *et al.*, "Onset of Hydrodynamic Mix in High-Velocity, Highly Compressed Inertial Confinement Fusion Implosions", Phys. Rev. Lett. 111, 085004 (2013).

[4.11] S. F. Khan *et al.*, "Measuring x-ray burn history with the Streaked Polar Instrumentation for Diagnosing Energetic Radiation (SPIDER) at the National Ignition Facility (NIF)", *Proc. SPIE* 8505, 850505 (2012).

[4.12] H. Herrmann *et al.*, "Diagnosing inertial confinement fusion gamma ray physics", Rev. Sci. Instrum. 81, 10D333 (2010).

[4.13] A. L. Kritcher *et al.*, "Integrated modeling of cryogenic layered highfoot experiments at the NIF", Phys. Plasmas **23**, 052709 (2016).

[4.14] D. S. Clark *et al.*, "Three-dimensional simulations of low foot and high foot implosion experiments on the National Ignition Facility", Phys. Plasmas **23**, 056302 (2016).

[4.15] S. W. Haan *et al.*, "Instability growth seeded by oxygen in CH shells on the National Ignition Facility", Phys. Plasmas 22, 032708 (2015).

[4.16] J. A. Frenje et al., "The magnetic recoil spectrometer (MRSt) for time-resolved measurements of the neutron spectrum at the National Ignition Facility (NIF)", Rev. Sci. Instrum. 87, 11D806 (2016).

Appendix A: Pictures

Figure A.1. Kyle Peterson from SNL giving an overview of the MagLIF concept to the NISP working group at the 1st NISP workshop in October 2015.

Figure A.2. Kyle Peterson from SNL answering a question about the MagLIF concept at the 1st NISP workshop in October 2015.

Figure A.3. Attendees at the 2nd NISP workshop in March 2016. The group consists of the NISP working group and invited experts on the different topics discussed at the 2nd workshop.

Figure A.4. Radha Bahukutumbi presenting the "Plans going forward to address the LDD knowledge gaps/hypotheses" to the NISP working group at the 4th workshop held in Washington D.C. on September 13-14, 2016.